https://doi.org/10.5194/egusphere-2023-418
Preprint. Discussion started: 23 March 2023

Internal tides off the Amazon shelf Part I: importance for the structuring of ocean temperature during two contrasted seasons

Fernand Assene [1], Ariane Koch-Larrouy [2], Isabelle Dadou [3], Michel Tchilibou [4], Guillaume Morvan [5], Jérôme Chanut [6], Vincent Vantrepotte [7], Damien Allain [8], Trung-Kien Tran [9].

[1, 2, 3, 5, 8] Université de Toulouse, LEGOS (CNRS/IRD/UPS/CNES), Toulouse, France, [1, 6] Mercator Ocean International, 31400 Toulouse, France, [4] Collecte Localisation Satellites (CLS), 31500 Ramonville Saint-Agne, France, [7, 9] Laboratoire d'Océanologie et de Géosciences (LOG), 62930 Wiméreux, France

Correspondence to: Fernand Assene (assene@legos.obs-mip.fr)

Abstract

Tides and internal tides (IT) in the ocean can significantly affect local to regional ocean temperature, including sea surface temperature (SST), via physical processes such as diffusion (vertical mixing) and advection (vertical and horizontal) of water masses. Offshore of the Amazon River, strong IT have been detected by satellite observations and well modelled; however, their impact on temperature, SST and the identification of the associated processes have not been studied so far. In this work, we use high resolution (1/36°) numerical simulations with and without the tides from an ocean circulation model (NEMO). This model explicitly resolves the internal tides (IT) and is therefore suitable to assess how they can affect ocean temperature in the studied area. We distinguish the analysis for two contrasted seasons, from April to June (AMJ) and from August to October (ASO), since the seasonal stratification off the Amazon River modulates the IT's response and their influence in temperature.

The generation and the propagation of the IT in the model are in good agreement with observations. The SST reproduced by the simulation including tides is in better agreement with satellite SST data compared to the simulation without tides. During ASO season, stronger meso-scale currents, deeper and weaker pycnocline are observed in contrast to the AMJ season. The observed coastal upwelling during ASO season is better reproduced by the model including tides, whereas the no-tide simulation is too warm by +0.3 °C for the SST. In the subsurface above the thermocline, the tide simulation is cooler by -1.2 °C, and warmer below the thermocline by +1.2 °C compared to the simulation without the tides. The IT induce vertical mixing on their generation site along the shelf break and on their propagation pathways towards the open ocean. This process mainly explains the cooler temperature at the ocean surface and is combined with vertical and horizontal advection to explain the cooling in the subsurface

water above the thermocline and a warming in the deeper layers below the thermocline. The surface cooling induced in turn an increase of the net heat flux from the atmosphere to the ocean surface, which could induce significant changes in the local and even for the regional tropical Atlantic atmospheric circulation and precipitation.

We therefore demonstrate that IT, via vertical mixing and advection along their propagation pathways, and tides over the continental shelf, can play a role on the temperature structure off the Amazon River mouth, particularly in the coastal cooling enhanced by the IT.

Keywords: internal tides, Amazon continental shelf and slope, temperature, modeling, satellite data, mixing, heat flux.

I. Introduction

Temperature and its spatial structure play a crucial role in ocean dynamics, including water mass formation (Swift and Aagaard, 1981; Lascaratos 1993; Speer et al. 1995), transport and mixing of other tracers in the ocean and exchanges with other biosphere compartments (Archer et al. 2004, Rosenthal et al. 1997), and most importantly on surface heat exchange at the interface with the atmosphere (Calyson and Bagdanoff, 2013; Mei et al. 2015) and can thus significantly influence the climate (Li et al. 2006; Collins et al. 2010). This oceanic thermal structure can be modified at various spatial and temporal scales by different processes external to the ocean such as incident solar radiation, heat fluxes with the atmosphere, winds, precipitation and freshwater inputs from rivers. Processes internal to the ocean also play a crucial role in this thermal structure, such as mass transport by currents and eddies (e.g.: Aguedjou et al., 2021), mixing by turbulent diffusion (Kunze et al. 2012), tides and internal tidal waves (IT) (Barton et al., 2001; Smith et al., 2016; Salamena et al., 2021). The role of IT on the thermal structure of the ocean is of increasing interest with many studies in recent years, but remains poorly understood in many ocean regions, and especially off the Amazon shelf.

In a stratified ocean, the passage of a barotropic tide over a topographic profile with a steep slope (continental slope, seamount, oceanic ridge) generates a disturbance in the flow that gives rise to a so-called baroclinic tide, with the same frequency, but with higher vertical velocities (Zhao et al., 2016). The baroclinic tide, also known as internal tidal waves (IT), thus captures part of the energy of the barotropic tide, propagates it and dissipates it into the global ocean by diapycnal mixing (Zhao et al., 2012), i.e., up to about 1 TW in the deep ocean (Egbert and Ray, 2000; Niwa and Hibiya, 2011) and thus helps to feed the thermohaline circulation (Munk and Wunsch, 1998). These two tidal processes (barotropic tide and IT) thus bring

https://doi.org/10.5194/egusphere-2023-418
Preprint. Discussion started: 23 March 2023

together a set of mechanisms for transferring and redistributing energy from larger to smaller oceanic scales, which can be understood as a tidal energy cascade. The dissipation of IT occurs mainly locally at the generation sites for high-mode IT that are associated with higher vertical shear, while a significant part of the energy dissipates offshore along their propagation path for low-mode IT (Zhao et al., 2016). Results from models in the Indonesian seas (Koch-Larrouy et al., 2007 and Nugroho et al., 2018) and observations in the Celtic Sea (Sharples et al. 2007) and the Yellow Sea (Xu et al., 2020), point out that IT dissipate most of their energy vertically, where the vertical gradient of stratification is maximal in the water column. IT can also vertically advect water masses during their propagation. They thus induce vertical displacements of the isopycnal levels of several meters to a few tens of meters, observable in the thermocline (Wallace et al., 2008; Xu et al. 2020). Denmann and Garett (1983) and Bordois et al. (2016) point out that the stratification peak acts as a waveguide for the propagation of IT.

The mixing and advection induced by IT results in a change in temperature structure throughout the water column. In surface waters, Smith et al. (2016) report that IT can induce surface cooling varying between 1 °C and 5 °C depending on the ocean region. Koch-Larrouy et al. (2007) and Nagai and Hibiya (2015) have shown, for the Indonesian region, that IT induces a surface cooling of -0.5 °C on average and that this decreases cloud convection in the atmosphere on a local scale, which in turn reduces precipitation by 20% and thus plays an important role on the climate on a regional scale. Furthermore, Jithin and Francis (2020) showed that IT can also affect the temperature in deep waters (> 1600 m), leading to a warming of the order of 1–2 °C.

The barotropic tides dissipate most of their energy in shallow coastal waters by bottom friction when the mean ocean depth becomes less than the amplitude of the tide (Lambeck and Runcorn, 1977; Le Provost and Lyard, 1997), and can thus modify temperature. Furthermore, Gonzalez-Haro et al. (2019) showed that barotropic and baroclinic tidal currents can induce temperature fluctuations by horizontal advection of surface water masses over hundreds of kilometers, and thus contribute to modifying the SST. These two tidal processes (barotropic and baroclinic) can also affect other tracers such as nutrients, chlorophyll and sediments (Heathershaw et al., 1987; da Silva et al., 2002; Sharples et al., 2007; Pomar et al., 2012; Muacho et al., 2014; Tuarena et al., 2016; Barbot et al., 2022).

Our study focuses on the oceanic region of northern Brazil off the Amazon River, where IT have been highlighted in previous studies, but their impact on the thermal structure is not currently known. This region is characterized by a broad, shallow continental shelf at the mouth

https://doi.org/10.5194/egusphere-2023-418
Preprint. Discussion started: 23 March 2023

of the Amazon River ended by a steep slope, i.e., a bathymetry variation of 200-2000 m over some tens of kilometers (Fig.1). Along this slope, six sites (A to F) of IT generation have been identified (Fig.1), the most intense of which (A and B) are in the south of the region (Magalhaes et al. 2016, Barbot et al. 2021 and Tchilibou et al. 2022). A strong seasonal coastal current, the Brazilian North Current (NBC), strongly influences the study area and flows along the coast from the southeast to the northwest (Johns et al., 1990).

This region shows a seasonal variation in the position of the winds and the Intertropical Convergence Zone (ITCZ) during the year, which directly influences the discharge of the Amazon River, the oceanic circulation (Xie and Carton, 2004), and therefore the stratification. This impacts the activity of internal tidal waves (Barbot et al., 2021). Two seasons can be clearly distinguished by their properties on water masses and currents.

The first season runs from March to July, during this time the ITCZ is in its most equatorial position and lies in the heart of our region. The increase in rainfall over the ocean leads to a colder and more homogeneous SST far from the coast. The discharge of the Amazon River into the ocean reaches its peak (> 3×10^5 $m^3.s^{-1}$) and the surface temperature in the coastal zone, although homogeneous, is warmer than offshore. At the end of this season, driven by the strong river discharge, the Amazon plume along the shelf extends beyond 8°N, and sometimes into the Caribbean region (Müller-Karger et al., 1989; Johns et al., 1998). The stratification is somewhat stronger and more homogeneous horizontally, and the maximum of its vertical gradient (pycnocline) is closer to the surface. This latter point leads to a stronger conversion of energy from barotropic to baroclinic, and a stronger local (first 50 km) dissipation of internal tidal wave energy (Barbot et al., 2021; Tchilibou et al., 2022). NBC and eddy kinetic energy (EKE) are weak in the region (Aguedjou et al., 2019). Close to the equator, the NBC develops a retroflection towards 1°N latitude that feeds the Equatorial Under-Current (EUC) transporting water masses eastwards to the Gulf of Guinea (Didden and Schott, 1993, Dimoune at al., 2022).

Contrasting with this first season, due to different oceanic and atmospheric conditions, the second season extends from August to December. During this season, the ITCZ migrates to its northernmost position around 10°N. In response, rainfall in this area decreases and the Amazon River discharge also decreases to its minimum (~ 10^5 $m^3.s^{-1}$), the extension of the river plume is therefore reduced to no more than 200–300 km offshore from the mouth of the Amazon between November and December (Johns et al., 1998, Garzoli et al., 2003). During this season, cold water (< 27.6 °C) associated with the western extension of the Atlantic cold-water tongue (ACT) enters the region from the south and runs along the edge of the continental shelf to about 3°N (Lentz and Limeburner, 1995; Neto et al., 2014), forming a cold cell often referenced as a seasonal upwelling. The stratification of the study area is strongly modified compared to the previous season. The pycnocline becomes somewhat deeper. The generation of IT on the slope and their local dissipation are weaker compared to the first season (Barbot et al., 2021; Tchilibou et al., 2022). Currents and eddy activity become stronger. The NBC becomes stronger, farther from the coast and deeper, it develops a retroflection (NBCR) between 5°–8° N that feeds the North Equatorial Counter-Current (NECC) transporting the water masses towards the east of the tropical Atlantic. This generates very large anticyclonic eddies (NBC Rings) exceeding 450 km in diameter (Didden and Schott, 1993; Richardson et al., 1994; Garzoli et al., 2004), which in turn transport water masses towards the Northern Hemisphere (Bourlès et al., 1999a; Johns et al., 1998; Schott et al., 2003). In addition, there are more cyclonic/anticyclonic eddies from the Gulf of Guinea during this season. All this contributes to the strengthening of the EKE, which reaches its maximum in this season (Aguedjou et al., 2019). When the baroclinic tidal flow interacts with the general circulation, it is deviated from its trajectory, thus we have a so-called incoherent baroclinic tide (Buijsman et al., 2017). This IT-circulation interaction is thus reinforced during this second season because of the more intensified currents and eddy activity (Tchilibou et al., 2022).

On the Brazilian continental shelf, Geyer et al. (1996) suggests the presence of internal tidal waves from current data. Later, Lentini et al. (2016) based on SAR imagery, shows small-wavelength (~ 10 km) internal solitary waves (ISW) packets propagating along and across the continental shelf, and generated by linear non-hydrostatic interactions between the NBC and barotropic tidal currents. Using a model, Molinas et al. (2020) show that baroclinic tidal currents play an important role on sediment transport on this continental shelf. On a global scale, several studies from altimetry observations (Zhao et al., 2012, 2016; Zaron et al., 2017, 2019) or models (Munk and Wunsch, 1998; Shriver et al., 2012; Arbic et al., 2012; Niwa and Hibiya, 2011, 2014; Buijsman et al. 2016) have shown intense activity of IT along the steep slope of the continental shelf. At the surface, using SAR imagery, Jackson (2007) and Magalhaes et al. (2016) describe longer wavelength ISW (~ 50–150 km) that propagate offshore from the slope. The latter emphasizes the modulation of their propagation by the seasonal variation of the NECC, and from a model, establishes that these ISW originate from instabilities and energy loss of IT coming from the slope, mainly at sites A and B. Recently, de Macedo et al. (2023) provided a somewhat more comprehensive description of the seasonal characteristics of these ISW, with the predominant origin remaining at sites A and B. Barbot

https://doi.org/10.5194/egusphere-2023-418
Preprint. Discussion started: 23 March 2023

et al. (2021) focused on the influence of stratification on the IT generation on the shelf as well as their propagation offshore. Finally, also in seasonal scale, Tchilibou et al. (2022) looked at the variation of the energy associated with IT from their generation to their dissipation, as well as the interaction of these waves with the general circulation. However, the interactions between IT and tracers such as temperature, salinity or chlorophyll have not received much interest from the scientific community in this region.

Hydrodynamic and biogeochemical conditions on the shelf and off the mouth of the Amazon were studied during the AMASSEDS campaigns in the early 1990s (DeMaster and Pope, 1996; Nittouer and DeMaster, 1996) and the various "*Camadas Finas*" campaigns (Araujo et al., 2017, 2021). Furthermore, using data from the two REVIZEE campaigns and TMI-SST satellite data, Neto et al. (2014) studied the seasonal cooling of surface waters, which occurs between the months of July and December. They conclude that the NBC is responsible for the upwelling of cold-water masses (< 27.5 °C) to the more superficial layers. Subsequently, Araujo et al. (2016), using in addition a realistic model, suggest that the tide would have a key role to play in intensifying this cooling. Indeed, through twin simulations with and without tide, they show that with tide there is a -0.3 °C cooling of the surface temperature. These analyses remain qualitative and do not allow determining what are the processes at work. Knowing that we are in an area with a strong activity of internal tidal waves, the question remains whether and by what processes these IT can structure the temperature both at the surface and inside the water column.

In order to answer the above questions, we used a high-resolution model (1/36°) and a satellite SST product, with the aim of highlighting the impact of IT on the temperature structure and associated processes. These observations, our modeling, as well as the methods used are described in section II. The validation of some barotropic and baroclinic tide's characteristics as well as SST are present in section III. The impacts of IT on the temperature structure, the influence on heat exchange at the interface between the atmosphere and the ocean, and finally the processes involved, are analyzed in section IV. Summary and discussions of the obtained results are presented in a last section.

II. Data and Methods

II.1. Satellite Data used: TMI SST

This dataset derived from Tropical Rainfall Measurement Mission (TRMM), which performs measurements using onboard TRMM Microwave Imager (TMI). The microwaves

https://doi.org/10.5194/egusphere-2023-418
Preprint. Discussion started: 23 March 2023

can penetrate clouds and are therefore very important for data acquisition in low latitude regions, cloudy covered during long periods of raining seasons. We use Remote Sensing Systems (RSS) TMI data products v7.1, which is the latest version of TMI SST. It contains a daily mean of SST with a 0.25°×0.25° grid resolution (~ 25 km). This SST is obtained by inter-calibration of TMI data with other microwave radiometers. The TMI SST fully description and inter-calibration algorithm is detailed in Wentz et al. (2015).

II.2. Model: *AMAZON36* configuration

The numerical model used in this study is the Nucleus for European Modelling of the Ocean (NEMOv4.0.2, Madec et al., 2019). The "*AMAZON36"* model configuration covers the western tropical Atlantic region with a 1/36° horizontal grid, from the Amazon River mouth to the open ocean. Several configurations with same grid resolution, but for the former NEMOv3.6 (Madec, 2014), exists for the same region, but either includes Caribbean Sea (Hernandez et al., 2016), or are not far extended to the east even used for tides study (Ruault et al., 2020). The present configuration is wider to capture, on their pathways, all the internal tide generating from the Brazilian shelf. Hence, the domain lies between 54.7°W–35.3°W and 5.5°S–10°N (Fig.1). In contrast with former configurations, we do not use multiple nested grids here, but a single grid. The vertical grid comprises 75 vertically fixed z-coordinates levels, finer grid refinement close to the surface with 23 levels in the 100 m, and cell thickness reaching 160 m when approaching the bottom. Both horizontal and vertical grid resolutions are therefore acceptable to resolve low-mode internal tides and were already used for that purpose (Tchilibou et al., 2022).

A third order upstream biased scheme (UP3) with built-in diffusion is used for momentum advection, while tracer advection relies on a 2nd order Flux Corrected Transport (FCT) scheme. A Laplacian isopycnal diffusion with a constant coefficient of 20 $m^2.s^{-1}$ is used for tracers. The temporal integration is achieved thanks to a leapfrog scheme combined with an Asselin filter to damp numerical modes (baroclinic time step is 150 s). The $k-\varepsilon$ turbulent closure scheme is used for the vertical diffusion coefficients. Bottom friction is quadratic with a bottom drag coefficient of 2.5×10^{-3}, while lateral wall free-slip boundary conditions are assumed. A time splitting technique is used to resolve the free surface, with the barotropic part of the dynamical equations integrated explicitly.

We use the General Bathymetric Chart of the Oceans (GEBCO, 2020) interpolated onto the model horizontal grid, with the minimal depth equal to 12.8 m. The ocean model is forced by the ERA-5 atmospheric reanalysis (Hersbach et al., 2020). The river discharges are based

https://doi.org/10.5194/egusphere-2023-418
Preprint. Discussion started: 23 March 2023

on monthly means from hydrology simulation of ISBA model (Interaction Sol-Biosphère-Atmosphère, see description in [ISBA - National Centre for Meteorological Research]), and are prescribed as surface mass sources with null salinity, and we use a multiplicative factor of 90% based on a comparison with the HYBAM interannual timeseries (HYBAM, 2018). The model is forced at its open boundaries by the fifteen major high-frequency tidal constituents (M2, S2, N2, K2, 2N2, MU2, NU2, L2, T2, K1, O1, Q1, P1, S1, and M4) and barotropic currents derived from FES2014 atlas (Lyard et al., 2021). At the open boundaries, we prescribe MERCATOR-GLORYS12 v1 (Lellouche et al., 2018) for temperature, salinity, sea level, current velocity and derived baroclinic velocity.

The simulation was initialized on the 1st of January 2005, and ran for 10 years until 2015. In this study, we use model outputs from 2013 to 2015. Indeed, the model has reached an equilibrium in terms of seasonal cycle after 2 years (2005-2006) of run. The same model configuration without the tides is used to highlight the influence of tides and IT on the temperature structure. To assess the realism of the model, we perform validation of various state variables used in this study such as the current's circulation, temperature, salinity, stratification as well as the barotropic and baroclinic tide properties.

II.3. Methods

II.3.1. Barotropic/baroclinic tide separation and tide energy budget

We follow Kelly et al. (2010) method to separate barotropic and baroclinic tide constituents: pressure, currents and energy flux. No modal separation is done, then tidal constituents obtained encompass the energy of all propagation's modes. Note that the barotropic/baroclinic tide separation is performed directly by the model for better accuracy, however, by this way it has the disadvantage of being very costly in terms of computing time. We therefore analyze only for one year (2015) the M2 frequency, since M2 is the major tidal constituent in this region, representing ~ 70% of the tidal energy (Beardsley et al., 1995; Gabioux et al., 2005 and Tchilibou et al., 2022).

The barotropic and baroclinic tide energy budget equations are obtained by ignoring as the first-order approximation the energy tendency, the nonlinear advection and the forcing terms (Wang et al., 2016). Then, the remaining equations are reduced to the balance between the divergence of the energy flux, the dissipation and the energy conversion from barotropic to baroclinic (Buijsman et al., 2017; Tchilibou et al., 2018, 2020, 2022; Jithin and Francis, 2020 ; Peng et al., 2021) :

$$D_{bt} + \nabla_h \cdot F_{bt} + CVR \approx 0 \qquad (\mathrm{W.m^{-2}}), \qquad (1)$$

https://doi.org/10.5194/egusphere-2023-418
Preprint. Discussion started: 23 March 2023

$$D_{bc} + \nabla_h \cdot F_{bc} - CVR \approx 0 \qquad (\text{W.m}^{-2}), \qquad (2)$$

bt and bc indicate the barotropic and baroclinic terms, D is the depth-integrated energy dissipation, which can be understood as a proxy of the real dissipation since D may encompass the energy loss of other tidal harmonics, non-linear terms and/or numerical dissipation (see Nugruho et al., 2018), $\nabla_h \cdot F$ represents the divergence of the depth-integrated energy flux, whilst CVR is the depth-integrated barotropic-to-baroclinic energy conversion, i.e. the amount of incoming barotropic energy which is converted into internal tides energy over the steep topography, with :

$$CVR = \langle \nabla H \cdot U_{bt}^{*} P_{bc}^{*} \rangle \qquad (\text{W.m}^{-2}), \qquad (3)$$

$$F_{bt} = \int_{H}^{\eta} \langle U_{bt}\, P_{bt} \rangle \, d_z \qquad (\text{W.m}^{-1}), \qquad (4)$$

$$F_{bc} = \int_{H}^{\eta} \langle U_{bc}\, P_{bc} \rangle \, d_z \qquad (\text{W.m}^{-1}), \qquad (5)$$

where the angle bracket denotes the average over tidal period, ∇H is the slope of the bathymetry, U_{bt}^{*} is the barotropic current and P_{bc}^{*} is the baroclinic pressure perturbation both at the bottom, H is the bottom depth, η the surface elevation, $U(u, \text{v})$ is the horizontal velocity, P is the pressure, then F is the energy flux and allows the propagation pathways of the given tide to be highlighted.

II.3.2. 3-D heat budget equation for temperature

The three-dimensional temperature budget was computed online and further analyzed. It is the balance between the total temperature trend and the sum of the temperature advection, diffusion and solar radiative and non-solar radiative fluxes (e.g.: Jouanno et al., 2011; Hernandez at al., 2017):

$$\partial_t T = \underbrace{-u\partial_x T - v\partial_y T - w\partial_z T}_{ADV} \underbrace{- \partial_z (Kz\partial_z T)}_{ZDF} + LDF_T + FOR_Z + Numdiff \qquad (°C.s^{-1}), \qquad (6)$$

Where T is the model potential temperature, $[u, v, w]$ are the space dimensional velocity components, ADV is the 3-D temperature advection (left to right: zonal, meridional and vertical terms), ZDF is the vertical diffusion, LDF_T is the lateral diffusion, FOR_z is the tendency of temperature due to penetrative solar radiation and has a vertical decaying structure. At the air-sea interface, the temperature flux is equal to the non-solar heat flux (sum of the latent, sensible and net infrared fluxes). FOR_z can modify temperature in the thin surface layer but will not be

https://doi.org/10.5194/egusphere-2023-418
Preprint. Discussion started: 23 March 2023

shown in the following. *Numdiff* corresponds to the sum of the numerical diffusion for the temperature. In this study, we assume that this last term is of second order and is not highlighted here.

II.3.3. The atmosphere–ocean net heat flux

The atmosphere–ocean net heat flux (Qt) reflects the balance of incoming and outgoing heat fluxes across the atmosphere-ocean interface (e.g.: Moisan and Niiler, 1998; Jayakrishnan and Babu, 2013), it is defined as follows:

$$Q_t = Q_{SW} \pm Q_{LW} \pm Q_{SH} \pm Q_{LH} \qquad W.m^{-2}, \qquad (7)$$

with from left to right: the incident solar radiative flux (Q_{SW}), the net infrared radiative flux (Q_{LW}), the incoming/outgoing sensible heat flux (Q_{SH}) which depends on the temperature difference between the atmosphere and the ocean surface, and the incoming/outgoing latent heat flux (Q_{LH}) which depends on the specific humidity difference between the atmosphere and the ocean surface. All these four components of the Qt influence the variation of the ocean surface temperature (SST). The last two components (Q_{SH} and Q_{LH}) have in addition a direct dependence relationship with the SST. Since IT can change the SST, we are therefore interested in knowing how it affects the net heat flux at the atmosphere-ocean interface.

III. Model validation

In this subsection we present for the M2 harmonic the barotropic and baroclinic tidal characteristics of the model for the year 2015, and the SST for the whole period from 2013 to 2015, and we verify that they agree with the different observations.

III.1. M2 Tides in the model

The barotropic SSH (Fig.2b) of the model is compared with FES2014 (Lyard et al. 2021) (Fig.2a), there is good agreement in terms of both amplitude and phase. Nevertheless, near the coast, some differences are observed in terms of amplitude. The SSH of the model is lower (~ +50 m) north of the mouth of the Amazon. However, inland and on the southern part of the mouth, the model overestimates the amplitude (~ +20 m and ~ +40 m respectively). This is in terms of order of magnitude like the biases in the Ruault et al. (2020) configuration that they compared to the FES2012 product (Carrère et al., 2012) over the same region. Along the steep slope of the bathymetry (see Fig.1), a portion of the incident barotropic tidal energy (black arrows Fig.2c and Fig.2d, for FES2014 and the model, respectively) in the presence of stratification is converted to baroclinic tidal energy. We compared the depth-integrated

https://doi.org/10.5194/egusphere-2023-418
Preprint. Discussion started: 23 March 2023

barotropic-to-baroclinic energy conversion rate (CVR) between the model (Fig.2d) and FES2014 (Fig.2c). The model does reproduce the same conversion patterns of FES2014 but can underestimate the CVR by about 30%. The bathymetry resolution plays a critical role in CVR (Niwa and Hibiya, 2011), then the difference in bathymetry resolution between the model (~ 3 km) and FES2014 (~ 1.5 km) could therefore explains that difference in CVR.

The critical slope for the M2 harmonic on the slope is greater than 1.2 (not shown), consequently, the baroclinic tides (internal tidal waves) thus generated will therefore propagate in the opposite direction to the barotropic tides, i.e., from the slope to the open ocean. The baroclinic tidal flux of the model (black arrows in Fig.2e) highlights the existence of six main sites of IT generation on the continental slope, two of which are more important (A and B), as shown by Maghalaes et al. (2016), Barbot et al. (2021) and Tchilibou et al. (2022). From these two main sites, the flow propagates offshore for nearly 1000 km. On its propagation path, the baroclinic tide signs at the surface in SSH. We compared this signature for the model (Fig.2h) with an estimate deduced from the altimeter tracks, produced by Zaron et al. (2019) (Fig.2g). The model is in good agreement with the altimetry observations, with an overestimation of the order of ~ +1.5 cm on the SSH maxima. It is important to note that the baroclinic SSH of the model is an average over the year 2015, whilst the observations are an average over about 20 years. This longer period may smooth the amplitude of the signal obtained from the altimetry observations. Also, the variability contained in the two averages is not the same, and this may explain some differences in the positioning and amplitude of the maxima.

Figure 2f shows the full depth-integrated internal tidal energy dissipation for the model. The estimated local dissipation of this energy is defined as follows:

$$P = (D_{bc} / CVR) * 100 \tag{8}$$

The local dissipation is then integrated at the embankment level in boxes A1, A2 and B (Fig.2f, see coordinates in Table-2 in Tchilibou et al. 2022) and provides information that a significant part of the energy is dissipated locally in the different boxes, i.e., about 30% (not shown). The local dissipation at the generation sites is thus in good agreement with Tchilibou et al. (2022). The remaining energy is exported offshore and dissipates along the propagation path. This dissipation is more extensive offshore along path A, ~ 500 km from the slope, with two patterns spaced approximately 120 km apart corresponding to propagation mode-1, and less extensive offshore along path B, ~ 100-200 km from the slope (Fig.2f).

https://doi.org/10.5194/egusphere-2023-418
Preprint. Discussion started: 23 March 2023

We have presented here only the dissipation for the M2 harmonic, but in the rest of the paper, we will analyze the temperature fields on a seasonal scale and by this fact, the effect of all the tidal harmonics on the temperature are considered.

III.2. SST Validation

Figure 3 shows the mean SST from TMI SST, tidal simulation and non-tidal simulation over the entire 2013-2015 period. The mean SST of the tidal simulation (Fig.3b) reproduces well spatially the TMI SST observations (Fig.3a) both for cooling on the shelf around 47.5°W and to the southeast between 40°W–35°W and 2°S–2°N, which is almost absent for the non-tidal simulation (Fig.3c). To the northeast, between 50°W–54°W and 3°N–8°N in the Amazon plume, the SST of the non-tidal simulation is in better agreement with the observations, while the SST of the tidal simulation is about -1 °C cooler than TIM SST. Such a difference is very similar to what is obtained by other models in the same region (Hernandez et al., 2016, 2017; Gévaudan et al., 2022). The seasonal cycle of the SST of the three products for the three years 2013-2015 (Fig.3d) is obtained by interpolating the SST of both simulations on the TMI SST grid and averaging in the dashed boxes around the IT generation areas (Fig.3a, b, and c) with the shelf being masked over the 200 m isobath. The tidal and non-tidal simulations of the model reproduce well both the seasonal cycle and the standard deviation of the observations, with a low RMSE of approximately 10^{-2} °C between each simulation and TMI SST (Fig.3d), which indicates the good quality of our model simulations. Nevertheless, over the seasonal cycle, it appears that between January-April and July-December, the tidal simulation is closer to the observations, while the non-tidal simulation seems slightly warmer than the observations; and in May-June, both simulations are colder than TMI SST (Fig.3d).

IV. Results

In this section, we will present the influence of IT on the SST, the associated processes, and the impact on the net atmosphere-ocean heat flux from the model's tidal and non-tidal simulations. The analyses were performed on a seasonal scale between April-May-June (AMJ) and August-September-October (ASO) for the three years 2013-2015.

IV.1. Tide-enhanced surface cooling

Beginning in July, a tongue of cold water (< 27 °C) begins to form to the southeast and enters the central part of the plateau in August and remains there until October. Figure 3e-g show the SST, averaged over the ASO season. The tidal simulation (Fig.3f) shows that the upwelling cell, represented by the extension of the 27.2 °C isotherm along the slope to about

https://doi.org/10.5194/egusphere-2023-418
Preprint. Discussion started: 23 March 2023

49°W–3°N, extends further north than in the non-tidal simulation (Fig.3g, 45°W–0°N) which is in better agreement with the TMI SST observations over the same period (Fig.3e).

The general impact of the tide, illustrated by showing the difference in SST between the tidal and the non-tidal simulations in both seasons (Fig.4c-d, respectively for AMJ and ASO), is a cooling over a large part of the study area with maxima (up to -0.3 °C): in the Amazon plume downstream of the river mouth (northeast beyond 3°N), and on the path of propagation of IT for both seasons. For ASO, tides induce a warming (> +0.3 °C) on the shelf at the mouth of the Amazon River, while for AMJ it is a cooling (-0.3 °C). East of 45°W, the tide-induced cooling for each of the two seasons has different spatial structures, but this is probably due to different mesoscale variability between the two seasons.

IV.2. Impact in the Atmosphere–Ocean Net heat flux (Q_T)

Associated with the cooling of the SST, the tide induces Qt anomalies whose spatial structure is very similar to the SST. Indeed, the difference in Qt is essentially positive over the whole domain during the AMJ season (Fig.4a) with average maximum values around 25 $W.m^{-2}$ in the plume and the Amazon retroflection to the northeast and along A and B. During the ASO season, there is as for the temperature at the mouth of the Amazon an inverse anomaly of (-25 $W.m^{-2}$) (Fig.4b). In each season, the spatial structure of the Qt difference almost perfectly matches that of the SST difference. Knowing that the atmosphere and the underlying ocean are in a certain equilibrium, the cooling of the SST by the water masses arriving at the surface will disturb this balance. In response, a consequent variation of the net heat flux from the atmosphere to the ocean, will try to restore the balance. As shown by the very strong and significant negative correlation between the difference in Qt and the difference in SST. For the AMJ season, we have a negative correlation of -0.97 with a significance of $R^2 = 0.95$, and about the same as for the ASO season with -0.98 and 0.96 respectively for negative correlation and its significance (Fig.9f).

The integral over the entire domain of the net heat flux for each season and for each simulation (Fig.4e) shows that during the AMJ season, the Qt increases from 23.85 TW for the non-tidal simulation to 35.7 TW for the tidal simulation, an increase of +33.2 %, two times greater than that found (15 %) by Tchilibou et al. (2020) in Solomon Sea. Thus, the tide and IT are responsible for a third of the variation in net atmosphere-ocean heat flux during this season. While during the second ASO season, there is a smaller increase in Qt of +7.4%, i.e., a variation from 73.03 TW to 78.83 TW between the non-tidal and tidal simulations.

https://doi.org/10.5194/egusphere-2023-418
Preprint. Discussion started: 23 March 2023

We also note the considerable difference in integrated Qt between seasons. We start from values below 36 TW in the AMJ season to values above 73 TW in the ASO season, i.e., a multiplication by a factor of at least order 2. These larger values could probably be related with the appearance of the upwelling cell described above, knowing that cooler SST induce stronger Qt.

IV.3. Vertical structure of the Temperature along A

To further analyze the temperature changes between both simulations, we made vertical sections following the path of IT emanating from sites A and B (blue and red line in Figure 2e respectively). We will show only the results following path A, but the results are similar for path B.

Figure 5 shows vertical sections of temperature for the two seasons following A. For the AMJ season, over the slope and near the coast, cold water (< 27.6 °C) remains below the surface at ~ 20 m for the tidal simulation (Fig.5a) and deeper at ~ 60 m for the non-tidal simulation (not shown), it then rises to the surface more than 400 km offshore for both simulations. Although at the surface the difference in SST between the two simulations (tide - no-tide) is relatively small (~ -0.3 °C, Fig.4c), because the SST is damped by the heat fluxes, further down the water column, this difference becomes much larger (> ± 1.2 °C, Fig.5c). Above the thermocline (< 120 m, cyan and yellow lines in Fig.5c), the simulation with the tides is colder by -1.2 °C from the slope where the IT are generated to the open ocean following their propagation path. Conversely, below the thermocline, the tidal simulation is warmer by +1.2 °C up to ~ 300 m along the same propagation path. During this AMJ season, the thermocline (~ 100 m ± 15 m, thick dashed black line, Fig.5a) and the mixing layer (~ 40 m ± 20 m, thick dashed white line, Fig.5a) have a very weak slope between the coast and the open ocean. Furthermore, the difference in isodensity depths between the two simulations is small (not shown), as are the depths of the thermocline (~ 10 m, Fig.5c) and the mixing layer (not shown), although these different depths are closer to the surface for the tidal simulation (not shown). Over the whole domain (not shown), the thermocline is deeper by 15 m on average in the non-tidal simulation, following the propagation paths of the IT energy flow, on the Amazon shelf and plume. While the mixing layer in the non-tidal simulation is deeper by an average of 13 m over the shelf, 4 m on average along the IT propagation paths and close to zero in the Amazon plume.

During the ASO season, cold waters (< 27.6 °C) previously confined below the surface during the previous season (AMJ) then rise to the surface. These cold waters extend over the

https://doi.org/10.5194/egusphere-2023-418
Preprint. Discussion started: 23 March 2023

slope and up to about 150 km offshore in the non-tidal simulation (not shown) and up to 250 km offshore in the tidal simulation (Fig.5b). The isotherm 27.2 °C reaches the surface above the slope in the tidal simulation but remains below the surface (~ 30 m) in the non-tidal simulation (not shown). At the surface and in the surface layers, the temperature in the presence of the tide and IT is therefore cooler. The temperature difference between the two simulations in the ASO season (Fig.5d) is smaller (< 0.4 °C) in the surface layers (< 40 m) near the coast compared to the AMJ season (Fig.5c). In contrast, during the ASO season, this cooling reaches the surface and results in a colder SST (-0.3 °C) (Fig.4d) along A. The strongest cooling (~ -1.2 °C) is deeper between 60 and 140 m depth. Below the thermocline, warming (+1.2 °C) is also present, but extends slightly less (~ 650 km) offshore (Fig.5d) compared to the AMJ season (~ 1000 km, Fig.5c). During this ASO season, the coastward slope of the thermocline and mixing layer becomes somewhat steeper compared to the other season. In both simulations, there is a dip of ~ 80 m (~60 m offshore and ~140 m inshore) and ~40 m (~30 m offshore and ~70 m inshore), respectively for the thermocline (thick dashed black line, Fig.5b) and the mixing layer (thick dashed white line, Fig.5b). Over the entire domain (not shown) between the two simulations (tide - no-tide), the tide deepens the thermocline depth by +6 m on the shelf and +12 m at the plume and along the propagation path of A. As for the mixing layer, which is deeper in the tidal run by 12 m along the shelf and along the propagation path of A.

Between the two seasons, there is also a change in the vertical density gradient between the coast and the open sea. In the simulation with tide (Fig.5a) and without tide (not shown), during the AMJ season, a strong vertical density gradient is present near the coast and decreases towards the open sea. In contrast, during the second ASO season, the vertical density gradient is weaker inshore than offshore. This clearly highlights a seasonality in the vertical density gradient profile in agreement with Tchilibou et al. (2022). The transect of the temperature differences between the two simulations (Fig.5c-d) show that IT (and probably the tide) can influence the temperature in the ocean from the surface to the bottom, with a greater effect on the first 300 meters. One question we address in this paper is to better understand what processes are at work that explain these temperature changes.

IV.4. Processes involved modifying the temperature

To explain the observed surface and water column temperature changes, we calculated the trend terms of the temperature evolution equation (see Section II.3.2, Equation 6) for both seasons (AMJ and ASO) also averaged over the three years from 2013 to 2015.

https://doi.org/10.5194/egusphere-2023-418
Preprint. Discussion started: 23 March 2023

IV.4.1. Vertical diffusion of Temperature

Figure 6 shows the vertical temperature diffusion term (ZDF) for both seasons AMJ (left panel) and ASO (right panel). The ZDF is averaged between 2–20 m, i.e., within the mixing layer depth range. For the AMJ season, the ZDF of the tidal simulation (Fig.6a) shows a negative trend (cooling) in the whole domain, which is maximum on the continental slope where the IT are generated and on their propagation path (< - 0.4 °C.day^{-1}), with larger horizontal extent along A (~700 km from the coasts) compared to B (~300 km from the coasts). Over the rest of the domain, it remains very low (> - 0.1 °C.day^{-1}). For the non-tidal simulation (Fig.6c), the ZDF is very weak (> - 0.1 °C.day^{-1}) over the entire domain, demonstrating that internal tidal waves would be the main driver of the vertical temperature diffusion in this region during this season. For the second ASO season, the tidal simulation (Fig.6b) shows a decrease of the ZDF along the coast and a strengthening offshore following A, but with the same cooling trend (< -0.4 °C.day-^{1}). While along B, it becomes almost closed to zero, both at the coast and offshore (Fig.6b). In addition, the mesoscale circulation intensifies during this season. Therefore, to the northeast, approximately between 4°N–8°N, and 47°W–53°W, there is a cooling on the shelf (~ +0.3 °C.day^{-1}) with NBCR-like patterns, both in the tidal simulation (Fig.6b) and in the non-tidal simulation (Fig.6d).

On the vertical following A, we notice an inter-thermocline vertical profile for the simulation with tide in the two seasons AMJ and ASO (respectively Fig.6e and 6f), with a cooling tendency (< -0.4 °C.day^{-1}) above the thermocline and a warming (> +0.4 °C.day^{-1}) below the thermocline, with an average vertical extension of ~ 350 m depth for the maximum values, but which exceeds 500 m depth for the low values (< +0.1 °C.day^{-1}). Over the slope, we see, as for the horizontal averages, this weakening of the ZDF between the AMJ (Fig.6e) and ASO (Fig.6f) seasons and the strengthening offshore. On the other hand, on the vertical, we observe towards the open sea (> 200 km) that the ZDF maxima seem to be discontinuous and spaced of about 120–150 km during the AMJ season (Fig.6e), while we have a more continuous diffusion for the ASO season (Fig.6f). This is consistent with the ZDF vertical averages (Fig.6a-b). For the non-tidal simulation, the vertical temperature diffusion tends towards 0 °C.day-^{1} within the water column but remains quite large (> -0.2 °C.day^{-1}) in the thin surface layer (Fig.6g-h).

During the AMJ season, the ITCZ is close to the equator and thus the trade Winds have their maximum intensity in the heart of the domain, while they migrate northward for the ASO season. As a result, more wind-generated diapycnal mixing is expected in the domain during

https://doi.org/10.5194/egusphere-2023-418
Preprint. Discussion started: 23 March 2023

the AMJ season compared to the ASO season. But the average value of the ZDF (~ -0.2 °C.day⁻¹) is the same between the two seasons and for both simulations (not shown) over most of the domain (except for the areas of the NBC backscatter for both simulations, on IT's generation sites and on their propagation path for the tidal simulation). This implies that the ability of the wind to generate diapycnal mixing in the underlying ocean surface layer could be limited by various oceanic processes in this region or is not well considered in the model.

Furthermore, it is important to note that along the IT propagation's pathway, the maximum of the ZDF follows the maxima of the baroclinic tidal energy dissipation (Fig.2f). Thus, the dissipation of IT generated on the continental slope generates vertical mixing that enhances the cooling observed at the surface along the coast. In addition, this temperature diffusion contributes to greater subsurface cooling, and warming in the deeper layers beneath the thermocline.

In section IV.3 the seasonality of the vertical gradient of stratification was highlighted, which is stronger at the coast relative to the open ocean during the AMJ season, and reverses during the ASO season to become stronger offshore relative to the coast. This could explain why the ZDF is stronger along the slope and along the near-coastal pathway B during the AMJ season (Fig.6a), while it is weaker along the slope and closed to zero following B during the ASO season (Fig.6b). The vertical gradient of density (and thus stratification) over the slope influences the generation of IT, by controlling the propagation mode of the IT that are generated (e.g.: Tchilibou et al., 2020 and Barbot et al., 2021). We show here that this vertical gradient also plays on the fate of these IT, in this case on their dissipation. The vertical gradient of the stratification thus determines where the internal tidal waves dissipate their energy in the water column.

IV.4.2. Vertical advection of Temperature

The vertical temperature advection (z–ADV) averaged between 2–20 m is almost zero in these surface layers throughout the region (Fig.7a, b, c, and d). For both seasons, some weak extreme values are in the northwest on the plateau between 54°W–50°W and 3°N–3°N) and are of the same intensity between the two simulations. With a slight intensification when moving to the ASO season (~ -0.3 °C.day⁻¹). The z–ADV is zero at the IT generation sites and along their propagation pathways, so the almost zero difference between the two simulations for each season shows that the IT and barotropic tide do not generate vertical temperature advection within these ocean surface layers. The z–ADV does not contribute to the temperature change in the surface layers of the ocean, and therefore does not influence the cooling observed

https://doi.org/10.5194/egusphere-2023-418
Preprint. Discussion started: 23 March 2023

from the surface on the SST. On the other hand, deeper, under the mixed layer and close to the thermocline, the z–ADV structure is more marked.

Vertical sections following A (Fig.7e, f, g and h) show an intensification of z–ADV below the mixing layer and near the thermocline between 80 and 200 m (~ ± 0.8 °C.day^{-1}). During the AMJ season, over the vertical, the z–ADV appears to be rather dominated by a cooling trend. The tidal simulation (Fig.7e) shows a cooling trend (~ -0.8 °C.day^{-1}), on the slope where the IT are generated, with an average vertical extension from ~ 20 to 200 m depth. Then offshore, two cooling hotspots (~ -0.8 °C.day^{-1}) followed by a weaker one (~ -0.3 °C.day^{-1}) spaced about 120–150 km apart, interspersed by two warming zones, respectively ~ +0.6 °C.day^{-1} and ~ +0.3 °C.day^{-1} from the coast. For the non-tidal simulation (Fig.7g), the z–ADV is much less intense with lower values (< ± 0.3 °C.day^{-1}) near the coast until ~ 300 km offshore, followed by a cooling hotspot (~ -0.8 °C.day^{-1}) between 300 km and 500 km. For both simulations, the extreme values appear to be centered around the mean depth of the thermocline (thick black outline) and do not cross the mixing layer depth (thick magenta outline). They are on average located between 40 m and 200 m depth and follow the position of the maximum vertical density gradient between isodensity anomalies 23.8–26.3 kg.m^{-3}.

For the ASO season, the simulation with tide (Fig.7f) still shows the same cooling intensity on the slope, although deeper (~ 60 m and 250 m), as well as offshore with this time the third cooling hotspot more intense (~ -0.8 °C.day^{-1}) than during the AMJ season (Fig.7e). The non-tidal simulation (Fig.7h) shows a less intense z–ADV (< ±0.1 °C.day^{-1}) near the slope, and a little stronger offshore (~ ±0.3 °C.day^{-1}) between 300 and 600 km from the slope, although less intense than the previous season.

As in the AMJ season, the extreme values of z–ADV follow the vertical density gradient in both simulations. During the ASO season, the maximum of the vertical density gradient is between 23.8 and 26.2 kg.m^{-3} and is deeper at the coast and is closer to the surface offshore. Thus, the extreme values of z–ADV are located a little deeper, between 80 and 300 m. Furthermore, for the non-tidal simulation and during both seasons, the position relative to the coast of the extreme values are shifted regarding those ones of the same polarity in the corresponding tidal simulation, which means that the presence of the IT and the tides could modify the intensity and patterns of the z–ADV produced by the other oceanic processes.

In addition, we averaged the z–ADV between deeper depths above the thermocline depth (20–70 m) and below the thermocline (148–250 m) depth for all simulations and both seasons (not shown). This allows to highlight the NBC's pathway through the extreme values

https://doi.org/10.5194/egusphere-2023-418
Preprint. Discussion started: 23 March 2023

of the z–ADV close to the coast and its retroflection offshore to the northeast for both simulations, but also the propagation of the IT from the coast to the open sea from the two main sites A and B for the simulation with tide. Thus, we see that the IT and the general circulation are the main drivers of the vertical temperature advection in the subsurface and deeper layers in this region.

IV.4.3. Horizontal advection of temperature

Horizontal advection of temperature (h–ADV) is defined as the sum of the zonal (x–ADV) and meridional (y–ADV) terms of temperature advection. The h–ADV is also averaged between 2–70 m for each simulation during both seasons (Fig.8a, b, c and d). As obtained with z–ADV, horizontal advection of temperature tends to zero over the entire domain in the surface layers for both seasons in both simulations, with some weak extreme values located in the northwest on the plateau between 54°W–50°W and 3°N–3°N) that intensify during the ASO season (~ ±0.2 °C.day^{-1}) (Fig.8b and d). Along the slope between sites A and B during the AMJ season, the h–ADV generates a small warming (~ +1 °C.day^{-1}) that is more pronounced in the tidal simulation (Fig.8a) than in the non-tidal simulation (Fig.8c), and thus appears to be related to the IT generated along the slope. On the other hand, the small difference between the two simulations in the surface layers shows that the tidal processes (IT and barotropic tide) hardly generate horizontal temperature advection. The low values observed here clearly show that the h–ADV could not influence the cold-water tongue observed over the surface SST (Fig.3e-g) during the ASO season.

Along the vertical following A, the h-ADV maxima remain essentially confined below the mixing layer, with much more intense values in the tidal simulation compared to the non-tidal simulation. The h–ADV contributes to both warming and cooling of the temperature (~ ±0.4 °C.day^{-1}) from the slope to more than 500 km offshore, with an average vertical extension between the surface and 400 m depth for the tidal simulation (Fig.8e and f) and a little less extended between 20–300 m depth for the non-tidal simulation (Fig.8g and h) during both seasons. The h–ADV which is low in the surface layers (2–20 m) but maximum in the subsurface where the stratification is stronger. We also see for the tidal simulation in both seasons a warming above the slope that reaches the surface with an intensity of about +0.4 °C.day^{-1} (Fig.8e and f) but remains below the surface (~ 20 m) in the non-tidal simulation (Fig.8g and h). This vertical excursion that is observed elsewhere for ZDF and z–ADV is a marker of local dissipation of IT at their generation site on the slope, which clearly affects both vertical diffusion and advection of the temperature. But we have almost null values along the

https://doi.org/10.5194/egusphere-2023-418
Preprint. Discussion started: 23 March 2023

slope when averaging h–ADV or z–ADV between 2-20 m and much more strong values for the ZDF (Fig.6a, b, c and d). This means that the IT's energy loss is mostly transferred to the turbulent scale (mixing). Furthermore, unlike the ZDF (Fig.6e) and z–ADV (Fig.7e and f), on the vertical it is difficult to identify a wave structure characteristic of IT propagation in the h-ADV.

V. Summary and Discussions

In this paper, the impact of internal tidal waves (IT) on temperature, off the Amazon, especially on the surface and on net heat fluxes is explored through outputs of two twin oceanic simulations (with and without tides) from a realistic model. The AMAZON36 configuration, based on the 1/36° resolution NEMO model, can reproduce the generation of internal tides (IT), i.e., the conversion of energy from barotropic to baroclinic tides, from two most energetic sites A and B, in good agreement previous studies (Magalhaes et al., 2016 and Tchilibou et al., 2022). As for dissipation, the model reproduces 30% local dissipation, the rest propagating offshore from the different generation sites, the two main ones being A and B (Fig.2e). During their propagation, the IT dissipate most of their energy after two beams of mode-1 reflection (120–150 km), that is less than 300 km from the slope.

The analyses are based on data from three years (2013 to 2015), averaged over two seasons, AMJ (April-May-June) and ASO (August-September-October) which are highly contrasted in terms of stratification, circulation and EKE. During ASO, the cold waters (< 27.5 °C) of the Atlantic Cold Tongue (ACT) enter our domain along the coast, and are affected by IT and tides, which leads to a cooler seasonal upwelling.

The impact of the tides on temperature was assessed by comparing our twin simulations with and without tides for each season. For ASO and AMJ, the tides create a cooling of SST of the order of ~ -0.3 °C in the plume of the Amazon offshore and along the paths of propagation A and B of the internal tide. Concerning the Amazon shelf, the tides induce a warming (~ +0.3 °C) in ASO and a cooling (of ~ -0.3 °C) in AMJ. These cooler/warmer waters are responsible in the same location for an increase/decrease in the net heat flux from the atmosphere to the ocean, leading to an increase (Qt) of +33.2% in AMJ and of +7.4% in ASO between runs with and without tides. In the subsurface, above the thermocline (<120 m), the IT and tides induce a stronger cooling than on the surface of about ~ -1.2 °C and an associated warming of about ~ +1.2 °C under the thermocline (>120 m to 300 m).

By increasing the atmosphere to ocean net heat flux (Qt), the IT and tides might reduce the cloud convection in the atmosphere, as we are in an intertropical convergence zone (ITCZ).

https://doi.org/10.5194/egusphere-2023-418
Preprint. Discussion started: 23 March 2023

Impact on overall atmospheric circulation and precipitation is expected to be significant, as previously shown in other regions such as Indonesia (Tidal induced cooling of -0.3 °C can reduce precipitation by -20%, see Koch-Larrouy et al., 2010).

Therefore, it becomes important to note that the interannual or even climatic scale evolution of internal tidal waves activity must be considered to better understand the future evolution of the global climate. Especially since thanks to the CanESM5 global climate model, Yadidya and Rao (2022) have just shown that in the Andaman Sea and Bay of Bengal, towards the end of this century, for both optimistic and pessimistic SSP scenarios, the increase in depth-averaged stratification will result in an increase in IT activity in these two regions. Knowing that the continental slope of northern Brazil is a place of high generation of IT, which therefore depends on stratification, it is hereby critical to understand how IT activity will evolve in the coming decades in order to better anticipate the climate, and thus better adapt public policies at national and international levels to the global context of climate change.

Another objective of our study was to understand the processes responsible for these temperature changes. For this, we analyzed the trend terms of the temperature evolution equation. Where IT dissipate their energy, there is an intense vertical mixing that generates vertical diffusion of temperature (ZDF) (-0.4 °C.day^{-1}) according to pathway A and to a lesser extent according to pathway B, stronger at shore than offshore during AMJ and inverse during ASO. The ZDF is the only process that reaches the surface layer, and then appears in first approximation to be the main process contributing to the surface cooling observed on SST. The atmospheric heat flux terms (FOR_Z) could also modify this SST but was not highlighted in this study. The mixing takes place up to about 800 km off the slope following A, and 300 km following B. It is also responsible on a seasonal scale, but also daily for a negative average variation (cooling) of temperature of about -0.4 °C.day^{-1} above the thermocline, and a warming of +0.4 °C.day^{-1} below 350 m and decreasing to +0.1 °C.day^{-1} around 500 m depth.

IT propagation induce vertical advection of water masses around the thermocline level, which has the effect of producing a subsurface mean temperature cooling (~ -0.8 °C.day^{-1}) at a depth varying between 20–200 m AMJ and 60–250 m in ASO, with three extreme values off the coast spaced approximately 120–150 km along of the pathway A, which seem to follow the dissipation patterns, and thus correspond to the horizontal scale of the mode-1 propagation of IT. Other processes such as zonal and meridional advection of temperature also induce temperature change in subsurface and deeper layers. Finally, the horizontal (zonal and

https://doi.org/10.5194/egusphere-2023-418
Preprint. Discussion started: 23 March 2023

meridional) advection of temperature in this region is more related to the general circulation (NBC, mesoscale) but is increased by tides and IT.

Thus, it is the combination of these different processes that explains the temperature change in the water column in this region. Furthermore, in order to explain the cooling of the SST at the surface, Neto et al. (2014) indicated that the northward transport of water masses by the constant circulation of the NBC was compensated by a vertical advection of colder water masses towards the surface. We now know that this vertical advection process fails to modify the SST but is rather limited below the mixing layer. The same is true for zonal and meridional advection of temperature (which form horizontal advection). It should be remembered that vertical diffusion extends from the surface, through the mixing layer, into the deep layers. It is therefore possible that water masses cooled by both vertical and horizontal advection below the mixing layer can be recovered and transported vertically to the surface by the effect of vertical mixing. The change in SST and temperature above the mixing layer then comes from (i) vertical diffusion of temperature and (ii) a combination of this vertical diffusion and the advection (vertical and horizontal) of temperature that takes place below the mixing layer.

This study focuses on temperature, but other analyses we have done on salinity show that IT also affects the haline structure of the ocean in this region. A future work would be to look at the impact on salinity, which is also a key parameter in the functioning of the ocean as in exchanges with the atmosphere, and thus can play a role on the climate. In addition, internal waves can also influence the biogeochemical cycles of elements and the entire marine ecosystem, since they can induce nutrient uptake and thus participate in structuring the spatial distribution of phytoplankton and zooplankton, and in consequence of the rest of the food chain that depends on them.

It would also be important to compare the results of our model with fields observations. Two high frequency PIRATA anchorages have been installed offshore at the extremity of our region between 35°W–38°W and 0°N–5°N (see Bourlès et al. 2019) and could be used for this purpose. In addition, recently, the "*AMAZOMIX*" campaign entirely dedicated to IT (27 August and 8 October 2021) will provide a better understanding of the impact of IT on the marine environment in this region. In the meantime, a coupled physical/biogeochemistry simulation (NEMO/PISCES), currently under analysis, will begin to answer these crucial questions of the impact of internal waves on biogeochemistry.

https://doi.org/10.5194/egusphere-2023-418
Preprint. Discussion started: 23 March 2023

Finally, in this first part, we have focused on describing the effects of internal tidal waves on temperature variation on a seasonal scale, while the remainder of this work will address temperature changes on finer time scales, notably on the tidal scale.

Data availability

The TMI SST v7.1 data are publicly available online from the REMSS platform: https://www.remss.com/missions/tmi/, was accessed on 27 June 2022. The model simulations are available upon request by contacting corresponding authors.

Authors contributions

Funding acquisition, AKL; Conceptualization and methodology, FA, AKL and ID. Numerical simulations, GM and FA. Formal analysis, FA; FA prepared the paper with contribution from all co-authors.

Competing interests

The authors declare that they have no conflict of interest.

Acknowledgments

This work is part of the Fernand Assene PhD thesis, cofounded by Institut de Recherche pour le Développement (IRD) and Mercator Ocean International (MOi). The numerical simulation was founded by CNRS/CNES/IRD via the projects A0080111357 and A0130111357 and were performed tank to the IDRIS platform calculator (Jean-Zay).

Abbreviations

The following abbreviations are used in this manuscript:

AMASSEDS: A Multi-disciplinary Amazon Shelf SEDiment Study

AMAZOMIX: AMAZOn MIXing

FES2012 | FES2014: Finite Element Solution 2012 | Finite Element Solution 2014

NEMO/PISCES: Nucleus for European MOdeling / Pelagic Interactions Scheme for Carbon and Ecosystem Studies

PIRATA: PredIction and Research moored Array in the Tropical Atlantic

REVIZEE : Recursos Vivos da Zona Econômica Exclusiva

https://doi.org/10.5194/egusphere-2023-418
Preprint. Discussion started: 23 March 2023

References

Aguedjou, H.M.A., Chaigneau, A., Dadou, I., Morel, Y., Pegliasco, C., Da-Allada, C.Y., Baloïtcha, E., 2021. What Can We Learn From Observed Temperature and Salinity Isopycnal Anomalies at Eddy Generation Sites? Application in the Tropical Atlantic Ocean. Journal of Geophysical Research: Oceans 126, e2021JC017630. https://doi.org/10.1029/2021JC017630

Aguedjou, H.M.A., Dadou, I., Chaigneau, A., Morel, Y., Alory, G., 2019. Eddies in the Tropical Atlantic Ocean and Their Seasonal Variability. Geophysical Research Letters 46, 12156–12164. https://doi.org/10.1029/2019GL083925

Araujo, M., Dimoune, D.M., Noriega, C., Hounsou-Gbo, G.A., Veleda, D., Araujo, J., Bruto, L., Feitosa, F., Flores-Montes, M., Lefèvre, N., Melo, P., Otsuka, A., Travassos, R.K., Schwamborn, R., Neumann-Leitão, S., 2021. Camadas Finas III - BR cruise: S-ADCP data. https://doi.org/10.17882/80828

Araujo, M., Noriega, C., Hounsou-gbo, G.A., Veleda, D., Araujo, J., Bruto, L., Feitosa, F., Flores-Montes, M., Lefèvre, N., Melo, P., Otsuka, A., Travassos, K., Schwamborn, R., Neumann-Leitão, S., 2017. A Synoptic Assessment of the Amazon River-Ocean Continuum during Boreal Autumn: From Physics to Plankton Communities and Carbon Flux. Frontiers in Microbiology 8.

Araujo, J.; Mezilet, Y.; Marin, F.; Jouanno, J.; Araujo, M. On the variability of the upwelling cell off the Amazon River mouth (01072-00001). In: VII Congresso Brasileiro de Oceanografia - CBO2016, 2016, Salvador, BA. Livro de Resumos - CBO2016. Salvador, BA: AOCEANO, 2016. v. 1.

Arbic, B., Richman, J., Shriver, J., Timko, P., Metzger, E., Wallcraft, A., 2012. Global Modeling of Internal Tides Within an Eddying Ocean General Circulation Model. Oceanography 25, 20–29. https://doi.org/10.5670/oceanog.2012.38

Archer, D., Martin, P., Buffett, B., Brovkin, V., Rahmstorf, S., Ganopolski, A., 2004. The importance of ocean temperature to global biogeochemistry. Earth and Planetary Science Letters 222, 333–348. https://doi.org/10.1016/j.epsl.2004.03.011

Barbot, S., Lagarde, M., Lyard, F., Marsaleix, P., Lherminier, P., Jeandel, C., 2022. Internal Tides Responsible for Lithogenic Inputs Along the Iberian Continental Slope. Journal of Geophysical Research: Oceans 127, e2022JC018816. https://doi.org/10.1029/2022JC018816

https://doi.org/10.5194/egusphere-2023-418
Preprint. Discussion started: 23 March 2023

Barbot, S., Lyard, F., Tchilibou, M., Carrere, L., 2021. Background stratification impacts on internal tide generation and abyssal propagation in the western equatorial Atlantic and the Bay of Biscay. Ocean Science 17, 1563–1583. https://doi.org/10.5194/os-17-1563-2021

Barton, E.D., Inall, M.E., Sherwin, T.J., Torres, R., 2001. Vertical structure, turbulent mixing and fluxes during Lagrangian observations of an upwelling filament system off Northwest Iberia. Progress in Oceanography, Lagrangian studies of the Iberian upwelling system 51, 249–267. https://doi.org/10.1016/S0079-6611(01)00069-6

Beardsley, R.C., Candela, J., Limeburner, R., Geyer, W.R., Lentz, S.J., Castro, B.M., Cacchione, D., Carneiro, N., 1995. The M2 tide on the Amazon Shelf. Journal of Geophysical Research: Oceans 100, 2283–2319. https://doi.org/10.1029/94JC01688

Bordois, L., Auclair, F., Paci, A., Dossmann, Y., Gerkema, T., Nguyen, C., 2016. Tidal energy redistribution among vertical modes in a fluid with a mid-depth pycnocline. Physics of Fluids 28, 101701. https://doi.org/10.1063/1.4964759

Bourles, B., Molinari, R.L., Johns, E., Wilson, W.D., Leaman, K.D., 1999. Upper layer currents in the western tropical North Atlantic (1989–1991). Journal of Geophysical Research: Oceans 104, 1361–1375. https://doi.org/10.1029/1998JC900025

Buijsman, M.C., Ansong, J.K., Arbic, B.K., Richman, J.G., Shriver, J.F., Timko, P.G., Wallcraft, A.J., Whalen, C.B., Zhao, Z., 2016. Impact of Parameterized Internal Wave Drag on the Semidiurnal Energy Balance in a Global Ocean Circulation Model. Journal of Physical Oceanography 46, 1399–1419. https://doi.org/10.1175/JPO-D-15-0074.1

Buijsman, M.C., Arbic, B.K., Richman, J.G., Shriver, J.F., Wallcraft, A.J., Zamudio, L., 2017. Semidiurnal internal tide incoherence in the equatorial Pacific. Journal of Geophysical Research: Oceans 122, 5286–5305. https://doi.org/10.1002/2016JC012590

Carrere, L., Lyard, F., Cancet, M., Guillot, A., & Roblou, L. (2012). FES 2012: A new global tidal model taking advantage of nearly 20 years of altimetry, in 20 Years of Progress in Radar Altimetry.

Clayson, C.A., Bogdanoff, A.S., 2013. The Effect of Diurnal Sea Surface Temperature Warming on Climatological Air–Sea Fluxes. American Meteorological Society.

Collins, M., An, S.-I., Cai, W., Ganachaud, A., Guilyardi, E., Jin, F.-F., Jochum, M., Lengaigne, M., Power, S., Timmermann, A., Vecchi, G., Wittenberg, A., 2010. The impact of global warming on the tropical Pacific Ocean and El Niño. Nature Geosci 3, 391–397. https://doi.org/10.1038/ngeo868

da Silva, J.C.B., New, A.L., Srokosz, M.A., Smyth, T.J., 2002. On the observability of internal tidal waves in remotely-sensed ocean colour data. Geophysical Research Letters 29, 10-1-10–4. https://doi.org/10.1029/2001GL013888

de Macedo, C.R., Koch-Larrouy, A., da Silva, J.C.B., Magalhães, J.M., Lentini, C.A.D., Tran, T.K., Rosa, M.C.B., Vantrepotte, V., 2023. Spatial and temporal variability of mode-1 and mode-2 internal solitary waves from MODIS/TERRA sunglint off the Amazon shelf. EGUsphere 1–27. https://doi.org/10.5194/egusphere-2022-1482

Demaster, D.J., Pope, R.H., 1996. Nutrient dynamics in Amazon shelf waters: results from AMASSEDS. Continental Shelf Research 16, 263–289. https://doi.org/10.1016/0278-4343(95)00008-O

Denman, K.L., Gargett, A.E., 1983. Time and space scales of vertical mixing and advection of phytoplankton in the upper ocean. Limnology and Oceanography 28, 801–815. https://doi.org/10.4319/lo.1983.28.5.0801

Didden, N., Schott, F., 1993. Eddies in the North Brazil Current retroflection region observed by Geosat altimetry. Journal of Geophysical Research: Oceans 98, 20121–20131. https://doi.org/10.1029/93JC01184

Dimoune, D. M., Birol, F., Hernandez, F., Léger, F., Araujo, M., 2022. Revisiting the tropical Atlantic western boundary circulation from a 25-year time series of satellite altimetry data. *EGUsphere*, 1-42.

Egbert, G.D., Ray, R.D., 2000. Significant dissipation of tidal energy in the deep ocean inferred from satellite altimeter data. Nature 405, 775–778. https://doi.org/10.1038/35015531

Gabioux, M., Vinzon, S.B., Paiva, A.M., 2005. Tidal propagation over fluid mud layers on the Amazon shelf. Continental Shelf Research 25, 113–125. https://doi.org/10.1016/j.csr.2004.09.001

Garzoli, S.L., Ffield, A., Johns, W.E., Yao, Q., 2004. North Brazil Current retroflection and transports. Journal of Geophysical Research: Oceans 109. https://doi.org/10.1029/2003JC001775

Garzoli, S.L., Ffield, A., Yao, Q., 2003. North Brazil Current rings and the variability in the latitude of retroflection, in: Goni, G.J., Malanotte-Rizzoli, P. (Eds.), Elsevier

https://doi.org/10.5194/egusphere-2023-418
Preprint. Discussion started: 23 March 2023

Oceanography Series, Interhemispheric Water Exchange in the Atlantic Ocean. Elsevier, pp. 357–373. https://doi.org/10.1016/S0422-9894(03)80154-X

Gévaudan, M., Durand, F., Jouanno, J., 2022. Influence of the Amazon-Orinoco Discharge Interannual Variability on the Western Tropical Atlantic Salinity and Temperature. Journal of Geophysical Research: Oceans 127, e2022JC018495. https://doi.org/10.1029/2022JC018495

Geyer et al., 1996. Physical oceanography of the Amazon shelf. Continental Shelf Research 16, 575–616. https://doi.org/10.1016/0278-4343(95)00051-8

González-Haro, C., Ponte, A., Autret, E., 2019. Quantifying Tidal Fluctuations in Remote Sensing Infrared SST Observations. Remote Sensing 11, 2313. https://doi.org/10.3390/rs11192313

Heathershaw, A.D., New, A.L., Edwards, P.D., 1987. Internal tides and sediment transport at the shelf break in the Celtic Sea. Continental Shelf Research 7, 485–517. https://doi.org/10.1016/0278-4343(87)90092-6

Hernandez, O., Jouanno, J., Durand, F., 2016. Do the Amazon and Orinoco freshwater plumes really matter for hurricane-induced ocean surface cooling? Journal of Geophysical Research: Oceans 121, 2119–2141. https://doi.org/10.1002/2015JC011021

Hernandez, O., Jouanno, J., Echevin, V., Aumont, O., 2017. Modification of sea surface temperature by chlorophyll concentration in the Atlantic upwelling systems. Journal of Geophysical Research: Oceans 122, 5367–5389. https://doi.org/10.1002/2016JC012330

Hersbach, H., Bell, B., Berrisford, P., Hirahara, S., Horányi, A., Muñoz-Sabater, J., Nicolas, J., Peubey, C., Radu, R., Schepers, D., Simmons, A., Soci, C., Abdalla, S., Abellan, X., Balsamo, G., Bechtold, P., Biavati, G., Bidlot, J., Bonavita, M., De Chiara, G., Dahlgren, P., Dee, D., Diamantakis, M., Dragani, R., Flemming, J., Forbes, R., Fuentes, M., Geer, A., Haimberger, L., Healy, S., Hogan, R.J., Hólm, E., Janisková, M., Keeley, S., Laloyaux, P., Lopez, P., Lupu, C., Radnoti, G., de Rosnay, P., Rozum, I., Vamborg, F., Villaume, S., Thépaut, J.-N., 2020. The ERA5 global reanalysis. Quarterly Journal of the Royal Meteorological Society 146, 1999–2049. https://doi.org/10.1002/qj.3803

https://doi.org/10.5194/egusphere-2023-418
Preprint. Discussion started: 23 March 2023

HYBAM (2018) Contrôles géodynamique, hydrologique et biogéochimique de l'érosion/altération et des transferts de matière dans les bassins de l'Amazone, de l'Orénoque et du Congo. http://www.ore-hybam.org. Accessed 10 December 2021

Jackson, C., 2007. Internal wave detection using the Moderate Resolution Imaging Spectroradiometer (MODIS). Journal of Geophysical Research: Oceans 112. https://doi.org/10.1029/2007JC004220

Jayakrishnan, P.R., Babu, C.A., 2013. Study of the Oceanic Heat Budget Components over the Arabian Sea during the Formation and Evolution of Super Cyclone, Gonu 2013. https://doi.org/10.4236/acs.2013.33030

Jithin, A.K., Francis, P.A., 2020. Role of internal tide mixing in keeping the deep Andaman Sea warmer than the Bay of Bengal. Sci Rep 10, 11982. https://doi.org/10.1038/s41598-020-68708-6

Johns, W.E., Lee, T.N., Beardsley, R.C., Candela, J., Limeburner, R., Castro, B., 1998. Annual Cycle and Variability of the North Brazil Current. Journal of Physical Oceanography 28, 103–128. https://doi.org/10.1175/1520-0485(1998)028<0103:ACAVOT>2.0.CO;2

Johns, W.E., Lee, T.N., Schott, F.A., Zantopp, R.J., Evans, R.H., 1990. The North Brazil Current retroflection: Seasonal structure and eddy variability. Journal of Geophysical Research: Oceans 95, 22103–22120. https://doi.org/10.1029/JC095iC12p22103

Jouanno, J., Marin, F., Du Penhoat, Y., Sheinbaum, J., & Molines, J. M., 2011. Seasonal heat balance in the upper 100 m of the equatorial Atlantic Ocean. Journal of Geophysical Research: Oceans, 116(C9).

Kelly, S.M., Nash, J.D., Kunze, E., 2010. Internal-tide energy over topography. Journal of Geophysical Research: Oceans 115. https://doi.org/10.1029/2009JC005618

Koch-Larrouy, A., Lengaigne, M., Terray, P., Madec, G., Masson, S., 2010. Tidal mixing in the Indonesian Seas and its effect on the tropical climate system. Clim Dyn 34, 891–904. https://doi.org/10.1007/s00382-009-0642-4

Koch-Larrouy, A., Madec, G., Iudicone, D., Atmadipoera, A., Molcard, R., 2008. Physical processes contributing to the water mass transformation of the Indonesian Throughflow. Ocean Dynamics 58, 275–288. https://doi.org/10.1007/s10236-008-0154-5

Koch-Larrouy, A., Madec, G., Bouruet-Aubertot, P., Gerkema, T., Bessières, L., Molcard, R., 2007. On the transformation of Pacific Water into Indonesian Throughflow Water

https://doi.org/10.5194/egusphere-2023-418
Preprint. Discussion started: 23 March 2023

by internal tidal mixing. Geophysical Research Letters 34. https://doi.org/10.1029/2006GL028405

Kunze, E., MacKay, C., McPhee-Shaw, E.E., Morrice, K., Girton, J.B., Terker, S.R., 2012. Turbulent Mixing and Exchange with Interior Waters on Sloping Boundaries. Journal of Physical Oceanography 42, 910–927. https://doi.org/10.1175/JPO-D-11-075.1

Lambeck, K., Runcorn, S.K., 1977. Tidal dissipation in the oceans: astronomical, geophysical and oceanographic consequences. Philosophical Transactions of the Royal Society of London. Series A, Mathematical and Physical Sciences 287, 545–594. https://doi.org/10.1098/rsta.1977.0159

Lascaratos, A., 1993. Estimation of deep and intermediate water mass formation rates in the Mediterranean Sea. Deep Sea Research Part II: Topical Studies in Oceanography 40, 1327–1332. https://doi.org/10.1016/0967-0645(93)90072-U

Le Provost, C., Lyard, F., 1997. Energetics of the M2 barotropic ocean tides: an estimate of bottom friction dissipation from a hydrodynamic model - ScienceDirect. Progress in Oceanography 37–52.

Lellouche, J.-M., Greiner, E., Le Galloudec, O., Garric, G., Regnier, C., Drevillon, M., Benkiran, M., Testut, C.-E., Bourdalle-Badie, R., Gasparin, F., Hernandez, O., Levier, B., Drillet, Y., Remy, E., Le Traon, P.-Y., 2018. Recent updates to the Copernicus Marine Service global ocean monitoring and forecasting real-time 1/12° high-resolution system. Ocean Science 14, 1093–1126. https://doi.org/10.5194/os-14-1093-2018

Lentini, C.A.D., Magalhães, J.M., da Silva, J.C.B., Lorenzzetti, J.A., 2016. Transcritical Flow and Generation of Internal Solitary Waves off the Amazon River: Synthetic Aperture Radar Observations and Interpretation. Oceanography 29, 187–195.

Lentz, S.J., Limeburner, R., 1995. The Amazon River Plume during AMASSEDS: Spatial characteristics and salinity variability. Journal of Geophysical Research: Oceans 100, 2355–2375. https://doi.org/10.1029/94JC01411

Li, C., Zhou, W., Jia, X., Wang, X., 2006. Decadal/interdecadal variations of the ocean temperature and its impacts on climate. Adv. Atmos. Sci. 23, 964–981. https://doi.org/10.1007/s00376-006-0964-7

Lyard, F.H., Allain, D.J., Cancet, M., Carrère, L., Picot, N., 2021. FES2014 global ocean tide atlas: design and performance. Ocean Science 17, 615–649. https://doi.org/10.5194/os-17-615-2021

https://doi.org/10.5194/egusphere-2023-418
Preprint. Discussion started: 23 March 2023

Madec, G., Bourdallé-Badie, R., Chanut, J., Clementi, E., Coward, A., Ethé, C., Iovino, D., Lea, D., Lévy, C., Lovato, T., Martin, N., Masson, S., Mocavero, S., Rousset, C., Storkey, D., Vancoppenolle, M., Müeller, S., Nurser, G., Bell, M., & Samson, G., (2019). NEMO ocean engine. In Notes du Pôle de modélisation de l'Institut Pierre-Simon Laplace (IPSL) (v4.0, Number 27). Zenodo. https://doi.org/10.5281/zenodo.3878122

Madec, G. (2014), "NEMO ocean engine" (Draft edition r5171), *Note du Pôle de modélisation 27*, Inst. Pierre-Simon Laplace, France, ISSN No 1288-1619.

Magalhaes, J.M., da Silva, J.C.B., Buijsman, M.C., Garcia, C. a. E., 2016. Effect of the North Equatorial Counter Current on the generation and propagation of internal solitary waves off the Amazon shelf (SAR observations). Ocean Science 12, 243–255. https://doi.org/10.5194/os-12-243-2016

Mei, W., Xie, S.-P., Primeau, F., McWilliams, J.C., Pasquero, C., 2015. Northwestern Pacific typhoon intensity controlled by changes in ocean temperatures. Science Advances 1, e1500014. https://doi.org/10.1126/sciadv.1500014

Moisan, J.R., Niiler, P.P., 1998. The Seasonal Heat Budget of the North Pacific: Net Heat Flux and Heat Storage Rates (1950–1990). Journal of Physical Oceanography 28, 401–421. https://doi.org/10.1175/1520-0485(1998)028<0401:TSHBOT>2.0.CO;2

Molinas, E., Carneiro, J.C., Vinzon, S., 2020. Internal tides as a major process in Amazon continental shelf fine sediment transport. Marine Geology 430, 106360. https://doi.org/10.1016/j.margeo.2020.106360

Muacho, S., da Silva, J.C.B., Brotas, V., Oliveira, P.B., 2013. Effect of internal waves on near-surface chlorophyll concentration and primary production in the Nazaré Canyon (west of the Iberian Peninsula). Deep Sea Research Part I: Oceanographic Research Papers 81, 89–96. https://doi.org/10.1016/j.dsr.2013.07.012

Muller-Karger, F.E., McClain, C.R., Richardson, P.L., 1988. The dispersal of the Amazon's water. Nature 333, 56–59. https://doi.org/10.1038/333056a0

Munk, W., Wunsch, C., 1998. Abyssal recipes II: energetics of tidal and wind mixing. Deep Sea Research Part I: Oceanographic Research Papers 45, 1977–2010. https://doi.org/10.1016/S0967-0637(98)00070-3

Nagai, T., Hibiya, T., 2015. Internal tides and associated vertical mixing in the Indonesian Archipelago. Journal of Geophysical Research : Oceans 120, 3373–3390. https://doi.org/10.1002/2014JC010592

Neto, A.V.N., da Silva, A.C., 2014. Seawater temperature changes associated with the North Brazil current dynamics. Ocean Dynamics 64, 13–27. https://doi.org/10.1007/s10236-013-0667-4

Nittrouer, C.A., DeMaster, D.J., 1996. The Amazon shelf setting: tropical, energetic, and influenced by a large river. Continental Shelf Research 16, 553–573. https://doi.org/10.1016/0278-4343(95)00069-0

Niwa, Y., Hibiya, T., 2014. Generation of baroclinic tide energy in a global three-dimensional numerical model with different spatial grid resolutions. Ocean Modelling 80, 59–73. https://doi.org/10.1016/j.ocemod.2014.05.003

Niwa, Y., Hibiya, T., 2011. Estimation of baroclinic tide energy available for deep ocean mixing based on three-dimensional global numerical simulations. J Oceanogr 67, 493–502. https://doi.org/10.1007/s10872-011-0052-1

Nugroho, D., Koch-Larrouy, A., Gaspar, P., Lyard, F., Reffray, G., Tranchant, B., 2018. Modelling explicit tides in the Indonesian seas: An important process for surface sea water properties. Marine Pollution Bulletin, Special Issue: Indonesia seas management 131, 7–18. https://doi.org/10.1016/j.marpolbul.2017.06.033

Peng, S., Liao, J., Wang, X., Liu, Z., Liu, Y., Zhu, Y., Li, B., Khokiattiwong, S., Yu, W., 2021. Energetics Based Estimation of the Diapycnal Mixing Induced by Internal Tides in the Andaman Sea. Journal of Geophysical Research: Oceans 126. https://doi.org/10.1029/2020JC016521

Pomar, L., Morsilli, M., Hallock, P., Bádenas, B., 2012. Internal waves, an under-explored source of turbulence events in the sedimentary record. Earth-Science Reviews 111, 56–81. https://doi.org/10.1016/j.earscirev.2011.12.005

Richardson, P.L., Hufford, G.E., Limeburner, R., Brown, W.S., 1994. North Brazil Current retroflection eddies. Journal of Geophysical Research: Oceans 99, 5081–5093. https://doi.org/10.1029/93JC03486

Rosenthal, Y., Boyle, E.A., Slowey, N., 1997. Temperature control on the incorporation of magnesium, strontium, fluorine, and cadmium into benthic foraminiferal shells from Little Bahama Bank: Prospects for thermocline paleoceanography. Geochimica et Cosmochimica Acta 61, 3633–3643. https://doi.org/10.1016/S0016-7037(97)00181-6

Ruault, V., Jouanno, J., Durand, F., Chanut, J., Benshila, R., 2020. Role of the Tide on the Structure of the Amazon Plume: A Numerical Modeling Approach. Journal of

https://doi.org/10.5194/egusphere-2023-418
Preprint. Discussion started: 23 March 2023

Geophysical Research: Oceans 125, e2019JC015495. https://doi.org/10.1029/2019JC015495

Salamena, G.G., Whinney, J.C., Heron, S.F., Ridd, P.V., 2021. Internal tidal waves and deep-water renewal in a tropical fjord: Lessons from Ambon Bay, eastern Indonesia. Estuarine, Coastal and Shelf Science 253, 107291. https://doi.org/10.1016/j.ecss.2021.107291

Schott, F.A., Dengler, M., Brandt, P., Affler, K., Fischer, J., Bourlès, B., Gouriou, Y., Molinari, R.L., Rhein, M., 2003. The zonal currents and transports at 35°W in the tropical Atlantic. Geophysical Research Letters 30. https://doi.org/10.1029/2002GL016849

Sharples, J., Tweddle, J.F., Green, J.A.M., Palmer, M.R., Kim, Y.-N., Hickman, A.E., Holligan, P.M., Moore, C.M., Rippeth, T.P., Simpson, J.H., Krivtsov, V., 2007. Spring-neap modulation of internal tide mixing and vertical nitrate fluxes at a shelf edge in summer. Limnology and Oceanography 52, 1735–1747. https://doi.org/10.4319/lo.2007.52.5.1735

Shriver, J., Arbic, B., Richman, J., Ray, R., Metzger, E., Wallcraft, A., Timko, P., 2012. An evaluation of the barotropic and internal tides in a high-resolution global ocean circulation model. Journal of Geophysical Research 117, C10024. https://doi.org/10.1029/2012JC008170

Smith, K.A., Rocheleau, G., Merrifield, M.A., Jaramillo, S., Pawlak, G., 2016. Temperature variability caused by internal tides in the coral reef ecosystem of Hanauma bay, Hawai‘i. Continental Shelf Research 116, 1–12. https://doi.org/10.1016/j.csr.2016.01.004

Speer, K.G., Isemer, H.-J., Biastoch, A., 1995. Water mass formation from revised COADS data. Journal of Physical Oceanography 25, 2444–2457.

Swift, J.H., Aagaard, K., 1981. Seasonal transitions and water mass formation in the Iceland and Greenland seas. Deep Sea Research Part A. Oceanographic Research Papers 28, 1107–1129. https://doi.org/10.1016/0198-0149(81)90050-9

Tchilibou, M., Koch-Larrouy, A., Barbot, S., Lyard, F., Morel, Y., Jouanno, J., Morrow, R., 2022. Internal tides off the Amazon shelf during two contrasted seasons: interactions with background circulation and SSH imprints. Ocean Science 18, 1591–1618. https://doi.org/10.5194/os-18-1591-2022

Tchilibou, M., Gourdeau, L., Lyard, F., Morrow, R., Koch Larrouy, A., Allain, D., Djath, B., 2020. Internal tides in the Solomon Sea in contrasted ENSO conditions. Ocean Science 16, 615–635. https://doi.org/10.5194/os-16-615-2020

Tchilibou, M., Gourdeau, L., Morrow, R., Serazin, G., Djath, B., Lyard, F., 2018. Spectral signatures of the tropical Pacific dynamics from model and altimetry: a focus on the meso-/submesoscale range. Ocean Science 14, 1283–1301. https://doi.org/10.5194/os-14-1283-2018

Tuerena, R.E., Williams, R.G., Mahaffey, C., Vic, C., Green, J.A.M., Naveira-Garabato, A., Forryan, A., Sharples, J., 2019. Internal Tides Drive Nutrient Fluxes into the Deep Chlorophyll Maximum Over Mid-ocean Ridges. Global Biogeochemical Cycles 33, 995–1009. https://doi.org/10.1029/2019GB006214

Wallace, M.I., Meredith, M.P., Brandon, M.A., Sherwin, T.J., Dale, A., Clarke, A., 2008. On the characteristics of internal tides and coastal upwelling behaviour in Marguerite Bay, west Antarctic Peninsula. Deep Sea Research Part II: Topical Studies in Oceanography 55, 2023–2040. https://doi.org/10.1016/j.dsr2.2008.04.033

Wang, X., Peng, S., Liu, Z., Huang, R.X., Qian, Y.-K., Li, Y., 2016. Tidal Mixing in the South China Sea: An Estimate Based on the Internal Tide Energetics. Journal of Physical Oceanography 46, 107–124. https://doi.org/10.1175/JPO-D-15-0082.1

Wentz, F.J., C. Gentemann, K.A. Hilburn, 2015: Remote Sensing Systems TRMM TMI [indicate whether you used Daily, 3-Day, Weekly, or Monthly] Environmental Suite on 0.25 deg grid, Version 7.1, [indicate subset if used]. Remote Sensing Systems, Santa Rosa, CA. Available online at www.remss.com/missions/tmi.

Xie, S.-P., Carton, J.A., 2004. Tropical Atlantic variability: Patterns, mechanisms, and impacts. Washington DC American Geophysical Union Geophysical Monograph Series 147, 121–142. https://doi.org/10.1029/147GM07

Xu, P., Yang, W., Zhu, B., Wei, H., Zhao, L., Nie, H., 2020. Turbulent mixing and vertical nitrate flux induced by the semidiurnal internal tides in the southern Yellow Sea. Continental Shelf Research 208, 104240. https://doi.org/10.1016/j.csr.2020.104240

Yadidya, B., Rao, A.D., 2022. Projected climate variability of internal waves in the Andaman Sea. Commun Earth Environ 3, 1–12. https://doi.org/10.1038/s43247-022-00574-8

Zaron, E.D., 2019. Baroclinic Tidal Sea Level from Exact-Repeat Mission Altimetry. Journal of Physical Oceanography 49, 193–210. https://doi.org/10.1175/JPO-D-18-0127.1

Zaron, E.D., 2017. Mapping the nonstationary internal tide with satellite altimetry. Journal of Geophysical Research: Oceans 122, 539–554. https://doi.org/10.1002/2016JC012487

Zhao, Z., Alford, M.H., Girton, J.B., Rainville, L., Simmons, H.L., 2016. Global Observations of Open-Ocean Mode-1 M2 Internal Tides. Journal of Physical Oceanography 46, 1657–1684. https://doi.org/10.1175/JPO-D-15-0105.1

Zhao, Z., Alford, M.H., Girton, J.B., 2012. Mapping Low-Mode Internal Tides from Multisatellite Altimetry. Oceanography 25, 42–51.

https://doi.org/10.5194/egusphere-2023-418
Preprint. Discussion started: 23 March 2023

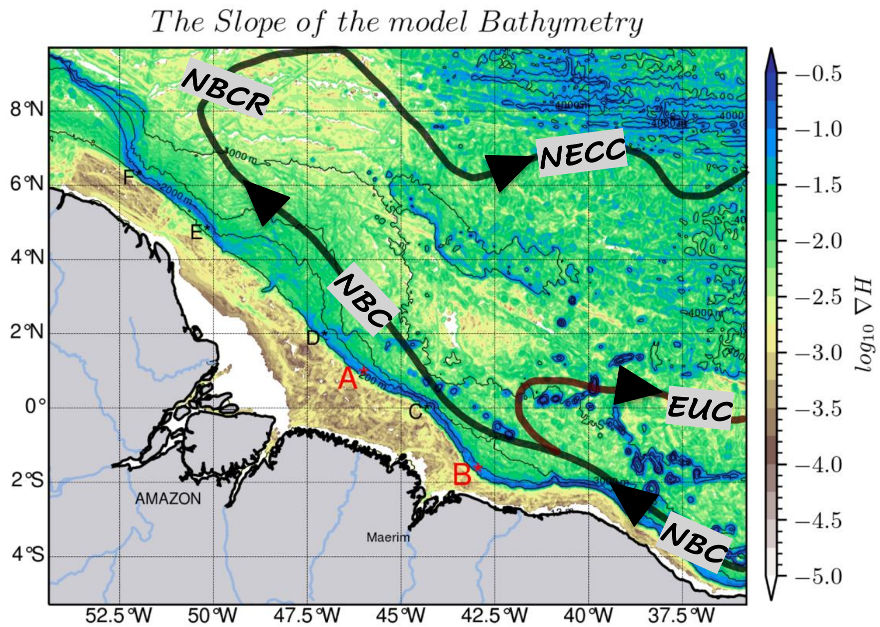

1098

1099 *Figure 1: The horizontal gradient (∇H) of the model's bathymetry with different internal*
1100 *tides generation sites (A*, B*, C*, D*, E* and F*) along the high slope (blue) of the shelf*
1101 *break, with the main sites (in red) being A* and B*, as mentioned in Magalhaes et al.*
1102 *(2016) and Tchilibou et al. (2022). Solid lines represent the circulation (as described by*
1103 *Didden and Schott, 1993; Richardson et al., 1994; Bourlès et al., 1999a; Johns et al.,*
1104 *1998; Schott et al., 2003; Garzoli et al., 2004) with NBC, NBCR and NECC pathways in*
1105 *black, and the EUC pathway in brown red. Tin black contours are 200 m, 2000 m, 3000*
1106 *m and 4000 m isobaths.*

https://doi.org/10.5194/egusphere-2023-418
Preprint. Discussion started: 23 March 2023

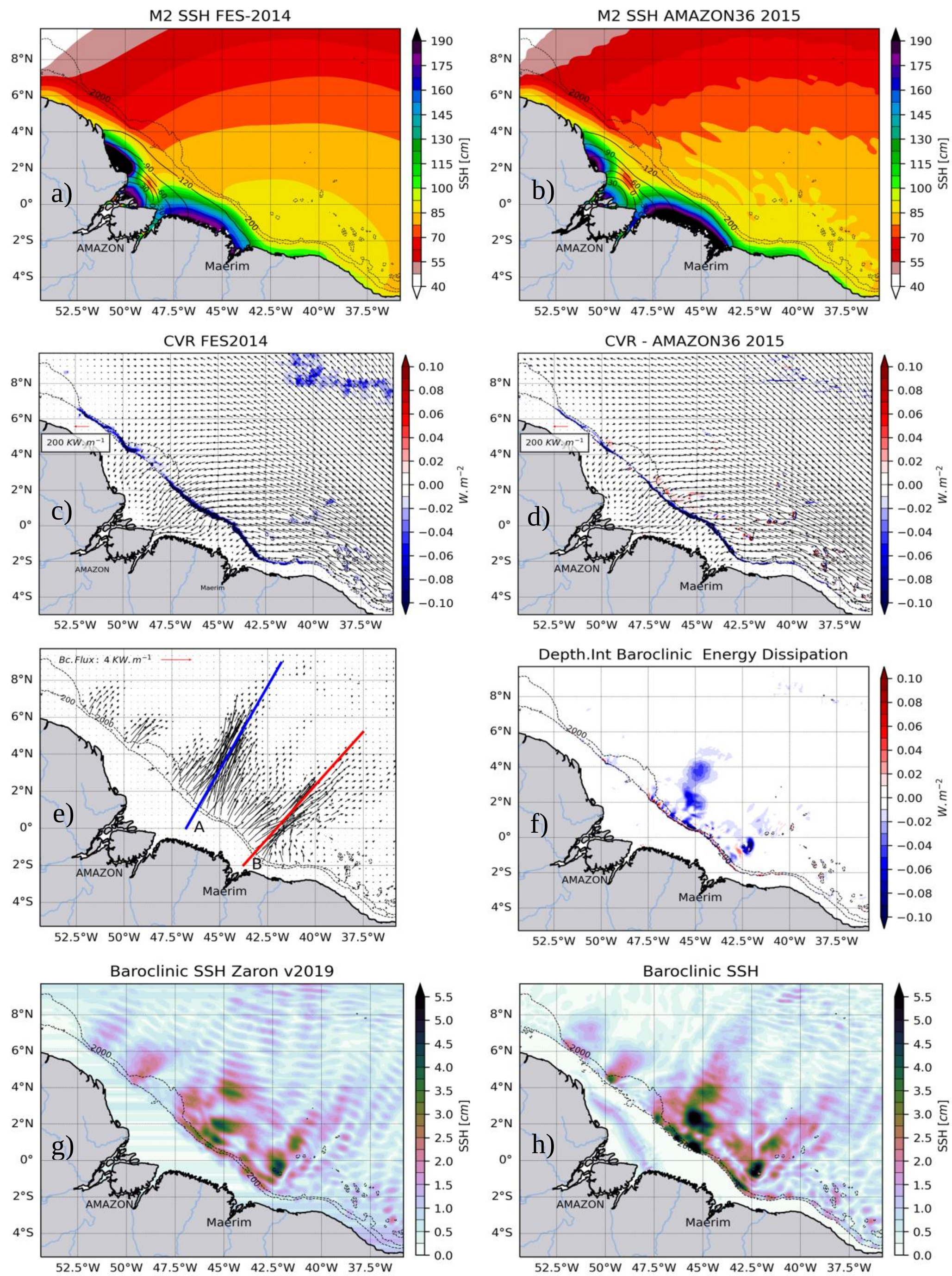

1113

https://doi.org/10.5194/egusphere-2023-418
Preprint. Discussion started: 23 March 2023

Figure 2: M2 tides (coherent) characteristics. Barotropic sea surface height for FES2014 (a) and model (b), depth-integrated energy conversion rate (CVR) (color shading) for FES2014 (c) and model (d) with barotropic energy flux black arrows, model depth-integrated baroclinic energy flux black (e) arrows with transect lines along A (blue) and B (red) IT's pathways, model depth-integrated baroclinic energy dissipation (f), and baroclinic sea surface height from observation (Zaron, 2019) (g) and model (h).

https://doi.org/10.5194/egusphere-2023-418
Preprint. Discussion started: 23 March 2023

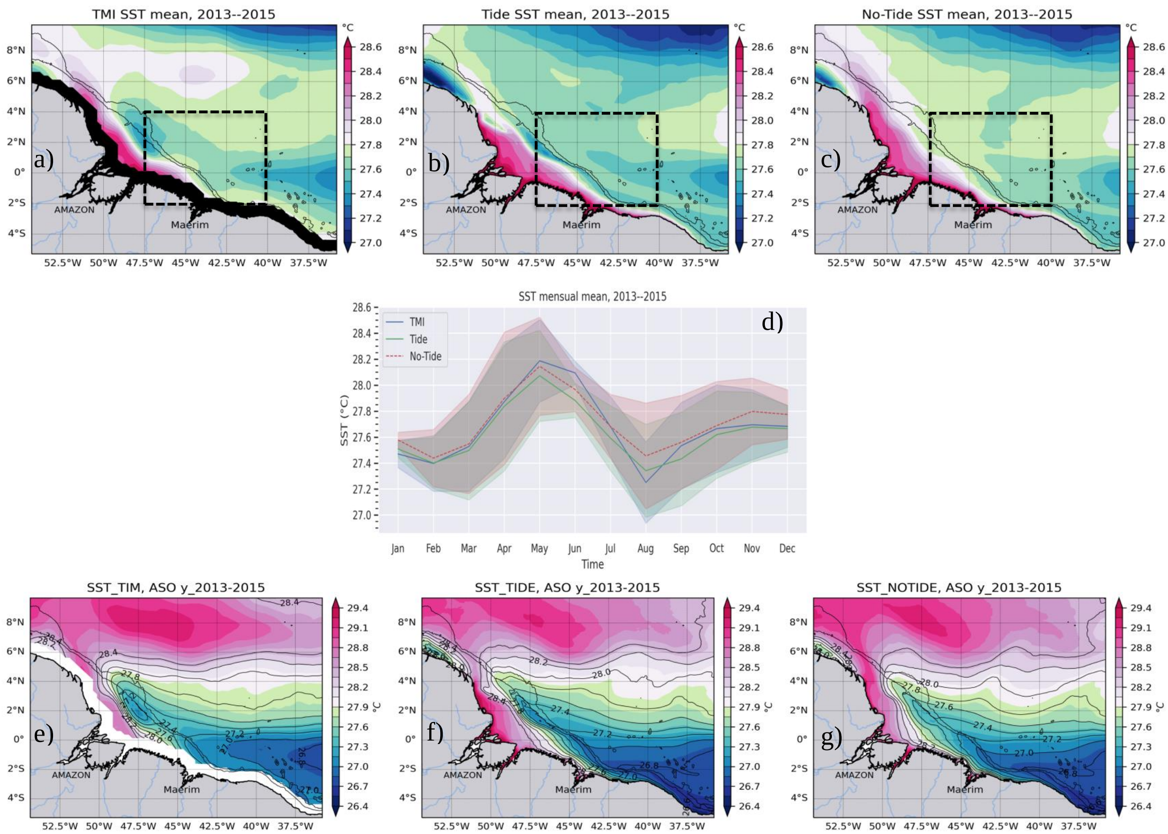

1136

https://doi.org/10.5194/egusphere-2023-418
Preprint. Discussion started: 23 March 2023

Figure 3: Mean SST for the period 2013 to 2015 from TMI SST (a) with a black coastal mask, the model's tidal simulation (b), the model's non-tidal simulation (c), seasonal cycle of the SST of the three products averaged inside the dotted line box (covering IT pathways emanating from the main generation sites A and B) with shelf masked over the 200 m isobath, the bands give the variability according to standard deviation (d). The lower panels present the SST averaged for the ASO (August-September-October) season over the years 2013–2015 for TMI SST (e) with a white coastal mask, the model's tidal simulation (f) and the model's non-tidal simulation (g), with the white thin lines representing the temperature contours. The black tin lines stand for the 200 m and 2000 m isobaths.

https://doi.org/10.5194/egusphere-2023-418
Preprint. Discussion started: 23 March 2023

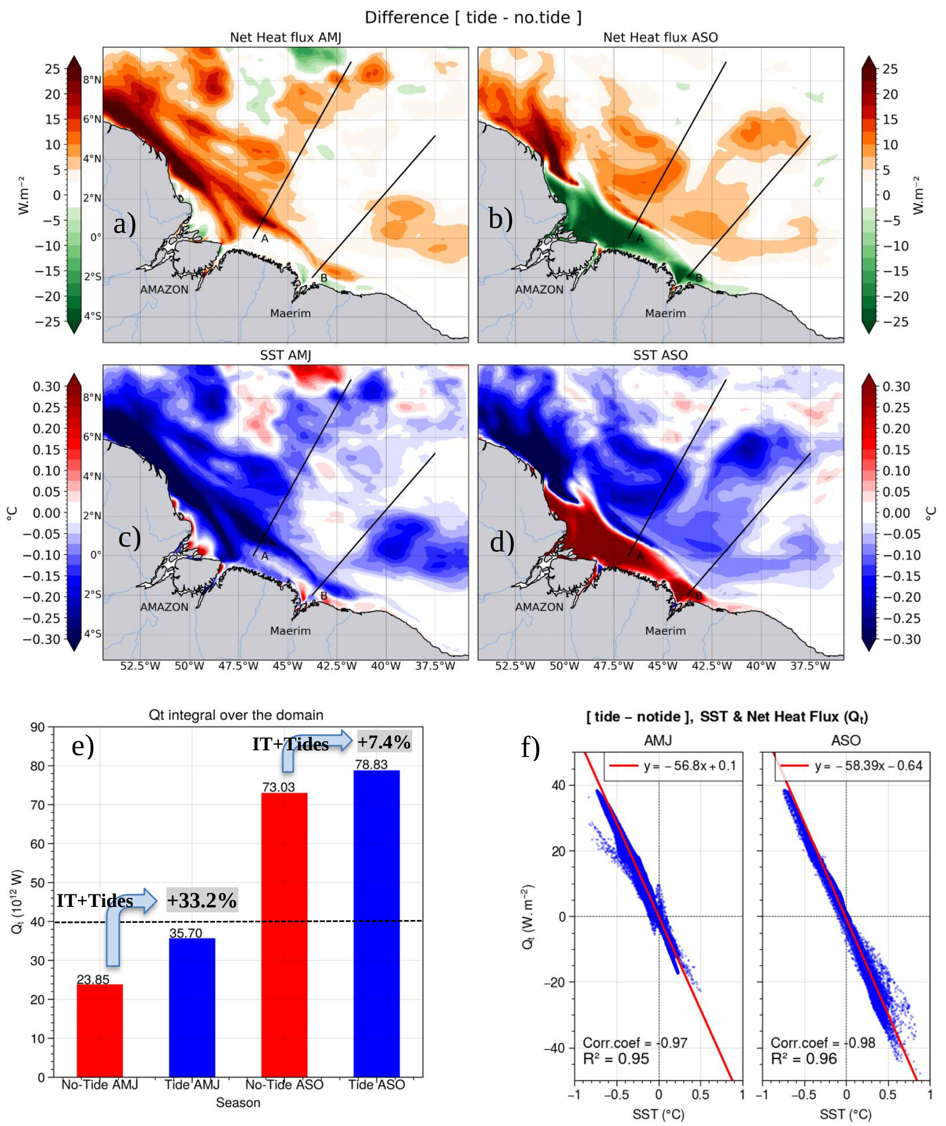

Figure 4: Relationship between the atmosphere-to-ocean net heat flux (Qt) and the SST: the Qt difference between tide and no-tide simulations in AMJ (a) and ASO (b) season, and SST difference in AMJ (c) and ASO (d), domain integrated Qt (e) for both seasons for each simulation. Correlation between Qt difference and SST difference for each season (f).

https://doi.org/10.5194/egusphere-2023-418
Preprint. Discussion started: 23 March 2023

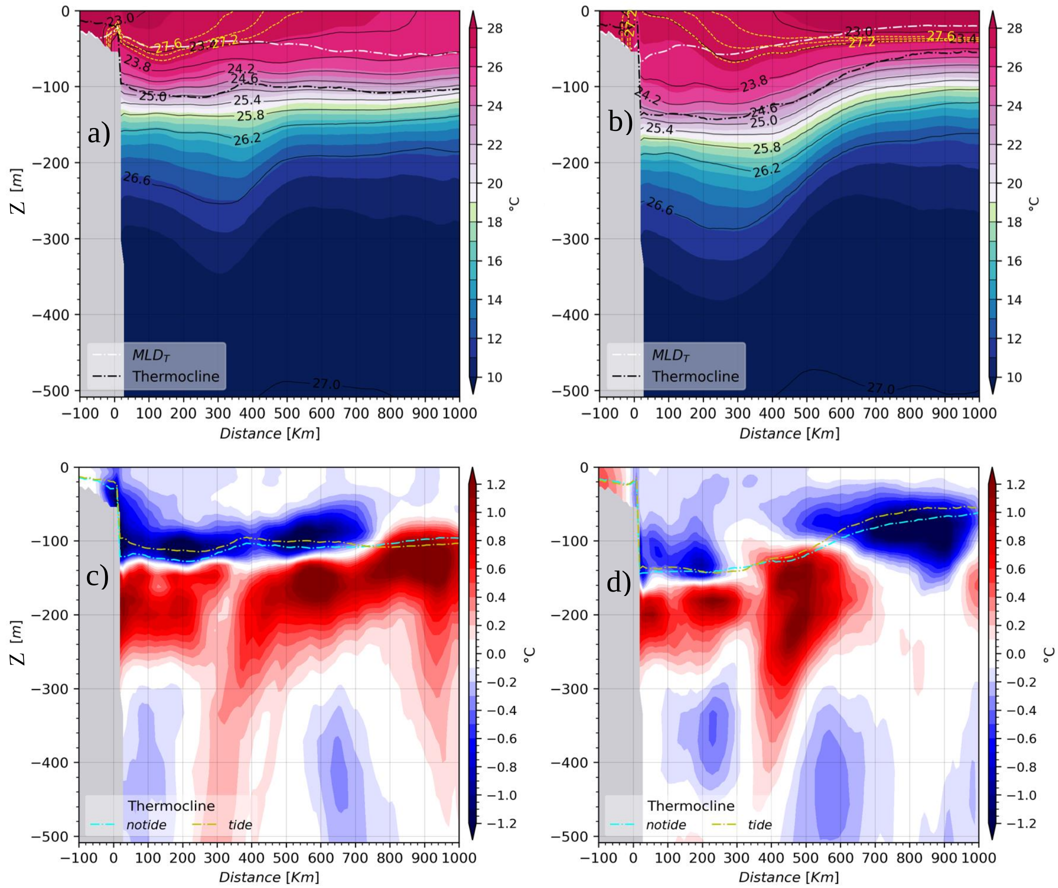

Figure 5: Vertical sections of tidal simulation's temperature following IT's pathway A for the AMJ (a) and ASO (b) seasons. Difference of temperature between tidal and non-tidal simulations for AMJ (c) and ASO (d) seasons. The yellow dotted and black tin lines in the upper panels are, respectively, for temperature and density anomaly isocontours, the black and white ticker dot-dashed lines are respectively thermocline and mixed layer depths. The yellow and cyan ticker dot-dashed lines in the lower panel are the thermocline depth respectively for tidal and non-tidal simulations.

https://doi.org/10.5194/egusphere-2023-418
Preprint. Discussion started: 23 March 2023

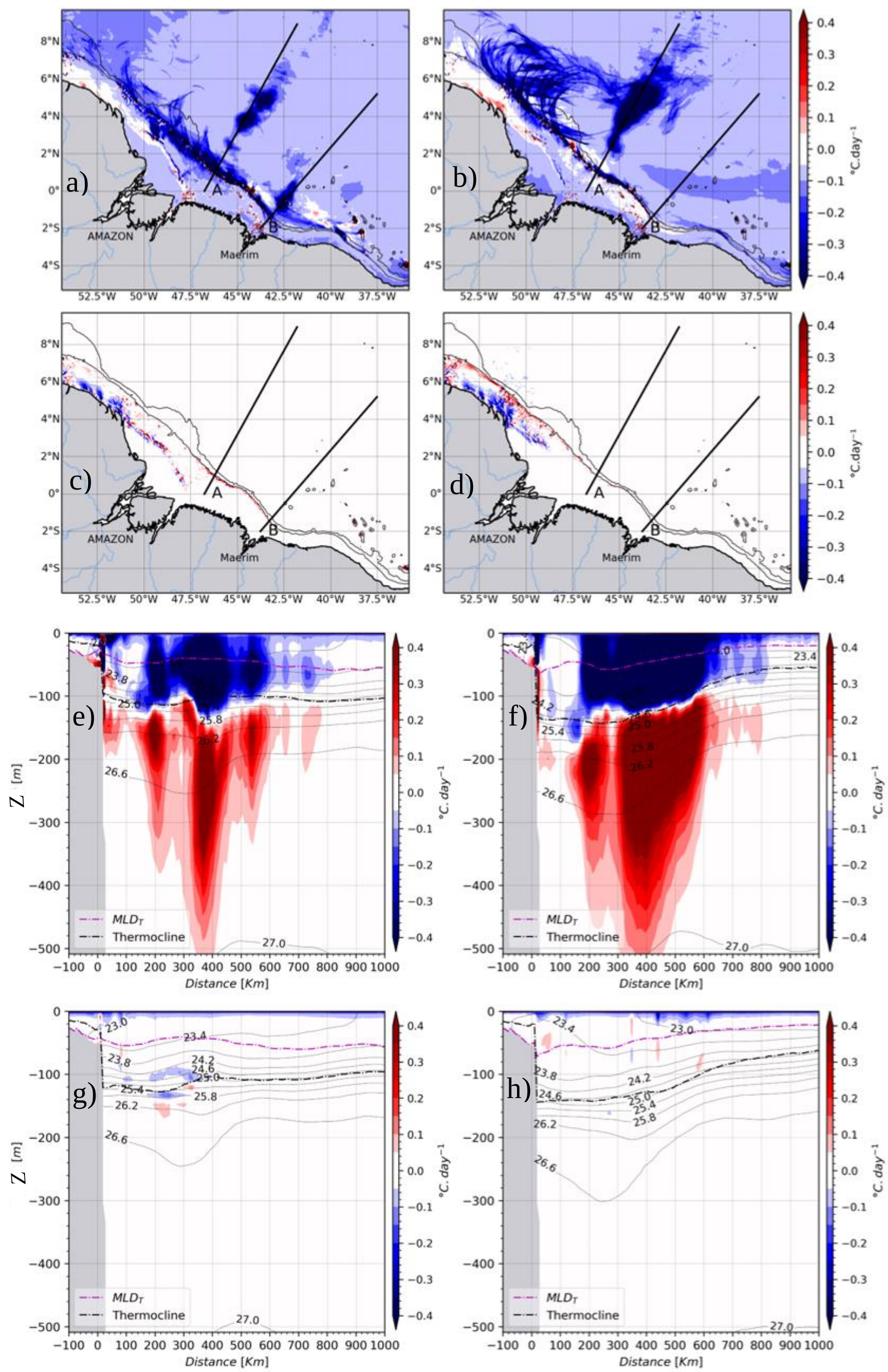

1180

1181 *Figure 6: The vertical diffusion of temperature (ZDF) for both seasons, respectively AMJ (left*

https://doi.org/10.5194/egusphere-2023-418
Preprint. Discussion started: 23 March 2023

panel) and ASO (right panel). Vertical mean between 2–20 m for AMJ season in tidal (a) and non-tidal (c) simulation; then for ASO season in tidal (b) and non-tidal (d) simulations. Black thin contours are, from the coast to open ocean, 200 m and 2000 m isobaths. Vertical section following A for AMJ season in tidal (e) and non-tidal (g) simulations; then for ASO season in tidal (f) and no-tidal (h) simulation. The black and magenta ticker dot-dashed lines are respectively thermocline depth and mixed layer depth. Thin black contours are for density anomaly.

https://doi.org/10.5194/egusphere-2023-418
Preprint. Discussion started: 23 March 2023

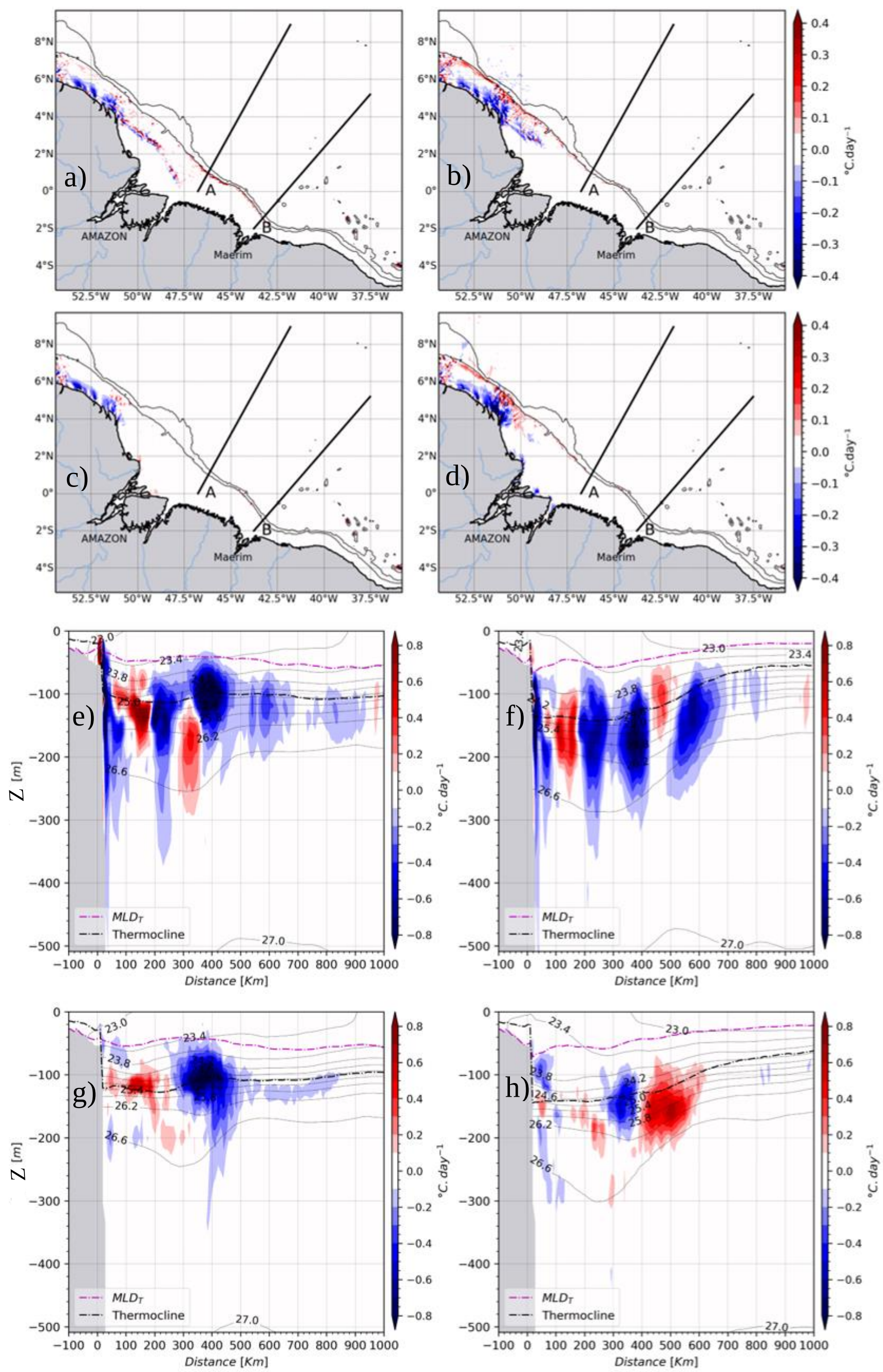

Figure 7: same as figure 6, but for the vertical advection of temperature (z–ADV).

https://doi.org/10.5194/egusphere-2023-418
Preprint. Discussion started: 23 March 2023

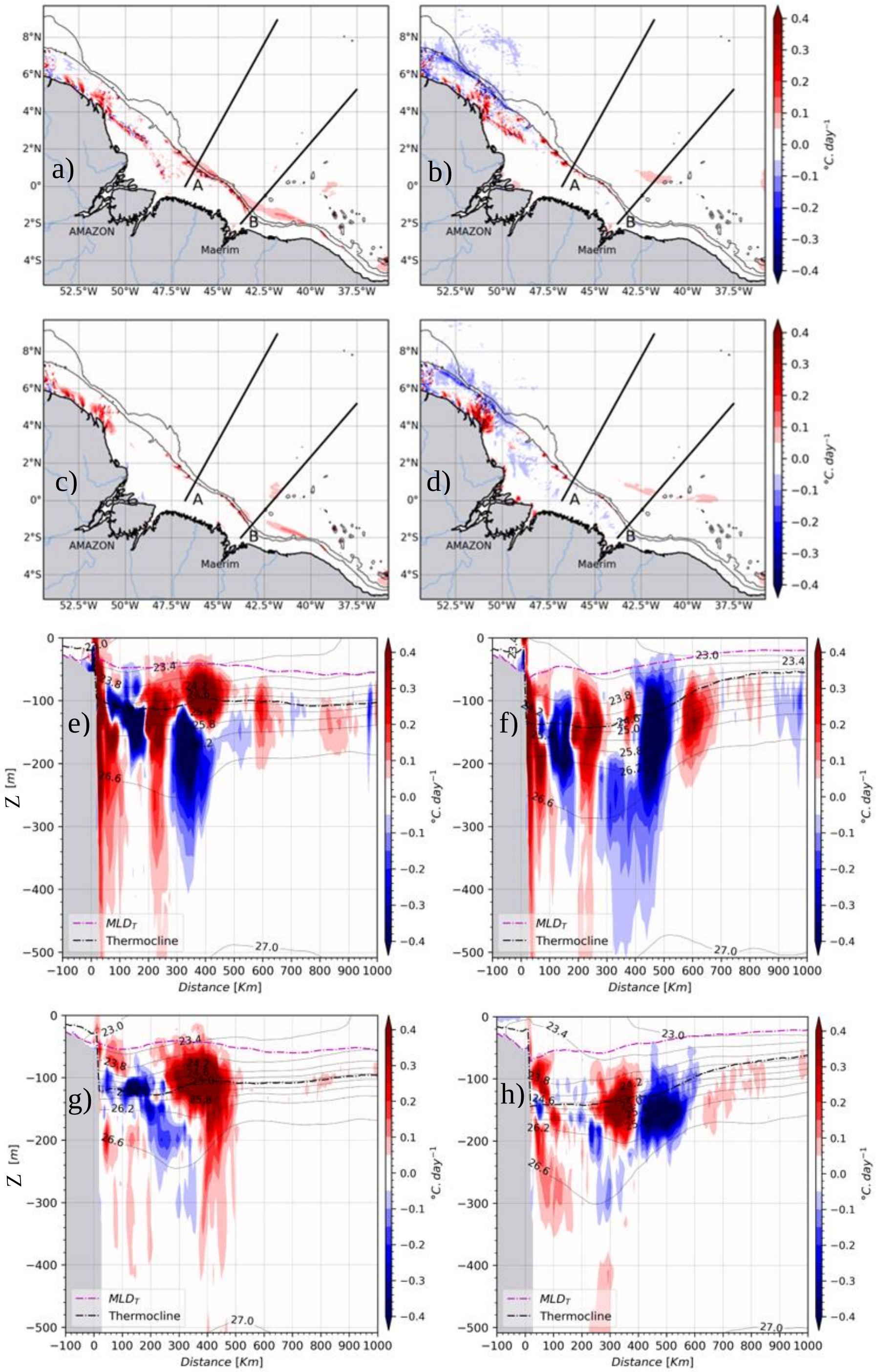

1206

1207 *Figure 8: same as figure 6 but for the horizontal advection of temperature (h-ADV = x–ADV*

https://doi.org/10.5194/egusphere-2023-418
Preprint. Discussion started: 23 March 2023

+ *y–ADV)*.